Lithos 208–209 (2014) 265–280

Contents lists available at ScienceDirect

Lithos

journal homepage: www.elsevier.com/locate/lithos

Lead transport in intra-oceanic subduction zones: 2D geochemical–thermo-mechanical modeling of isotopic signatures

Bettina Baitsch-Ghirardello [a], Andreas Stracke [b], James A.D. Connolly [a], Ksenia M. Nikolaeva [c], Taras V. Gerya [a,d,*]

[a] Department of Earth Sciences, Swiss Federal Institute of Technology (ETH-Zurich), Sonneggstrasse, 5, 8092 Zurich, Switzerland
[b] Institut für Mineralogie, Westfälische Wilhelms-Universität Münster, Germany
[c] Institute Cluster Earth & Climate, Department of Earth Sciences, Faculty of Earth and Life Sciences, Vrije Universiteit Amsterdam, de Boelelaan 1085, 1081 HV Amsterdam, Netherlands
[d] Geology Department, Moscow State University, 119899 Moscow, Russia

ARTICLE INFO

Article history:
Received 31 July 2014
Accepted 10 September 2014
Available online 22 September 2014

Keywords:
Intra-oceanic subduction
Serpentinization
Pb isotopic signature
Numerical modeling

ABSTRACT

Understanding the physical–chemical mechanisms and pathways of geochemical transport in subduction zones remains a long-standing goal of subduction-related research. In this study, we perform fully coupled geochemical–thermo-mechanical (GcTM) numerical simulations to investigate Pb isotopic signatures of the two key "outputs" of subduction zones: (A) serpentinite mélanges and (B) arc basalts. With this approach we analyze three different geodynamic regimes of intra-oceanic subduction systems: (1) retreating subduction with backarc spreading, (2) stable subduction with high fluid-related weakening, and (3) stable subduction with low fluid-related weakening. Numerical results suggest a three-stage Pb geochemical transport in subduction zones: (I) from subducting sediments and oceanic crust to serpentinite mélanges, (II) from subducting serpentinite mélanges to subarc asthenospheric wedge and (III) from the mantle wedge to arc volcanics. Mechanical mixing and fluid-assisted geochemical transport above slabs result in spatially and temporarily variable Pb concentrations in the serpentinized forearc mantle as well as in arc basalts. The Pb isotopic ratios are strongly heterogeneous and show five types of geochemical mixing trends: (i) binary mantle–MORB, (i) binary MORB–sediments, (iii) double binary MORB–mantle and MORB–sediments, (iv) double binary MORB–mantle and mantle–sediments and (v) triple MORB–sediment–mantle. Double binary and triple mixing trends are transient and characterize relatively early stages of subduction. In contrast, steady-state binary mantle–MORB and MORB–sediments trends are typical for mature subduction zones with respectively low and high intensity of sedimentary melange subduction. Predictions from our GcTM models are in agreement with Pb isotopic data from some natural subduction zones.

1. Introduction

The mechanisms and pathways of geochemical transport in subduction zones are of fundamental importance to understand global geochemical cycles. Consequently, one of the long-standing goals of subduction-related geochemical studies is to determine how and where subducted components are redistributed between various crustal and mantle reservoirs (e.g., King et al., 2007). The geodynamic "inputs" to the subduction factory include subducted oceanic crust and sedimentary rocks, whereas the easily accessed "outputs" comprise volcanics and plutonics of magmatic arcs and various exhumed subduction-related metamorphic rock complexes and tectonic mélanges (e.g., Kelley et al., 2005; King et al., 2007; Marschall and Schumacher, 2012; Plank and Langmuir, 1993, 1998; Scambelluri et al., 2004 and references therein). Investigation and comparison of the inputs and outputs of the subduction factory produced a number of predictions regarding the role of metamorphic, magmatic and fluid processes in redistributing geochemical components during subduction (e.g., Behn et al., 2011; Chauvel et al., 1995; Kelley et al., 2005; Marschall and Schumacher, 2012; Scambelluri and Tonarini, 2012; Scambelluri et al., 2004; Tamura et al., 2011). Quantitative testing of these predictions requires observational constraints (e.g., King et al., 2007; Marschall and Schumacher, 2012; Scambelluri and Tonarini, 2012) and realistic subduction models coupled to geochemical processes (e.g., Behn et al., 2011; Gerya, 2011a; Kimura et al., 2009, Vogt et al., 2013).

Of particular importance for the geochemical subduction cycle is how dehydration and hydration affect element transport in the forearc and subarc regions. Slab dehydration releases large volumes of aqueous fluids (Schmidt and Poli, 1998), which trigger partial melting in the mantle wedge at ~80–150 km depth (Bebout et al., 1999). At shallower

* Corresponding author at: Department of Earth Sciences, Swiss Federal Institute of Technology (ETH-Zurich), Sonneggstrasse, 5, 8092 Zurich, Switzerland. Tel.: +41 44 633 66 23; fax: +41 44 633 10 65.
E-mail address: taras.gerya@erdw.ethz.ch (T.V. Gerya).

http://dx.doi.org/10.1016/j.lithos.2014.09.006
0024-4937/

depths of the forearc region, released fluids cause hydration and serpentinization of the overlying mantle peridotites (e.g., Bostock et al., 2002; Scambelluri and Tonarini, 2012). Serpentinization of the forearc mantle lithosphere is a multi-stage process, which plays a fundamental role for geochemical cycling in subduction zones (e.g. Deschamps et al. 2010; Elliott, 2003; Elliott et al., 1997; Hyndman and Peacock, 2003; Ruepke et al., 2004; Scambelluri and Philippot, 2001; Scambelluri et al. 2001a, 2001b; Ulmer and Trommsdorff, 1995). Slab-derived fluids become incorporated with their typical geochemical signature in the serpentinized layers, which have lowered rheological strength and decreased density compared to their peridotites protolith (Bostock et al., 2002; Escartín et al., 2001; Furukawa, 1993; Hilairet et al., 2007; Iwamori, 1998). The serpentinized mantle layer where up to >13% water is stored (Ulmer and Trommsdorff, 1995) is able to transport chemically bound water to a greater mantle depth when it is dragged downward by subduction-induced flow (e.g., Hattori and Guillot, 2003; Ruepke et al., 2004; Tatsumi, 1989). It is then possible that trace elements such as Pb, which are released at relatively low temperature, reach substantially greater depths than expected (Hattori and Guillot, 2003; King et al., 2006, 2007; Kodolányi et al., 2012; Scambelluri and Tonarini, 2012; Scambelluri et al., 2004). Indeed, a sediment signature of mobile elements such as Pb is found in nearly all intra-oceanic magmatic arcs (e.g., Hauff et al., 2003; Ishizuka et al., 2003, 2006; Plank and Langmuir, 1993; Straub et al., 2010).

Serpentinite minerals form in the relatively cold forearc mantle wedge but become unstable at higher temperatures in the subarc and backarc, where breakdown of hydrous minerals releases an aqueous fluid phase (e.g., Hyndman and Peacock, 2003; Iwamori, 1998; Iwamori et al., 2007; Tatsumi, 1989). A waning fluid flux with depth decreases the amount of fluid mobile elements (Ishikawa and Nakamura, 1994). Therefore, there is a smaller Pb concentration in serpentinites at depths where arc magmas are generated (Hyndman and Peacock, 2003). The host lithology of the releasing fluids also changes with depth (e.g. Iwamori, 1998). In the forearc wedge fluids are mostly derived from sediments, whereas they derive from altered oceanic crust at greater depth (Ishikawa and Nakamura, 1994), and from dehydrated serpentinites in the lower wedge. Furthermore, serpentinite mélange formation in the forearc is an intrinsic subduction-related process, which imposes significant controls on the geochemistry of subduction zone fluids and magmatic arc products (e.g., Castro and Gerya, 2008; King et al., 2006, 2007; Marschall and Schumacher, 2012; Scambelluri et al., 2004). The chemical–mechanical origin of the mélange formation implies that comparisons of end-member subduction "inputs" to arc volcanic "outputs" for inferring recycling at subduction zones may over-simplify the physics and chemistry of the mass transfer in subduction zones, as subducted mass is consistently redistributed into novel hybrid bulk compositions (King et al., 2006). Such mélange zones along the slab–mantle interface simultaneously bear characteristic elemental or isotopic signals of several distinct input lithologies, and experience metamorphic and melting reactions that are not typical of any of the end-member lithologies (Castro and Gerya, 2008; Castro et al., 2010; King et al., 2006). Therefore, observational, experimental and numerical modeling studies should explore geochemical and magmatic consequences of such hybridized systems for understanding geochemical evolution of subduction zones (e.g., Castro and Gerya, 2008; Castro et al., 2010; King et al., 2006, 2007; Marschall and Schumacher, 2012; Scambelluri et al., 2004).

In the last two decades, hydration/dehydration processes in the mantle wedge have been actively modeled numerically (Gerya, 2011a,b and references therein). The pioneering work of Davies and Stevenson (1992) was one of the first subduction modeling studies aimed at simulating the water transport in the mantle wedge beneath volcanic arcs. Based on a simple slab dehydration model, it was proposed that the combination of vertical percolation of water and the solid-state transport of hydrated mantle by the mantle wedge flow, can lead to the net horizontal transport of water from the cold subducting slab into the hot subarc interior of the mantle wedge.

Iwamori (1998, 2000, 2004) and Iwamori et al. (2007) created a self-consistent numerical model of subduction that included slab dehydration, water transport, mantle hydration and melting of the mantle wedge. In this numerical model, the aqueous fluid migrated by porous flow and interacted chemically with the moving solid mantle wedge rocks. The calculations (Iwamori, 1998; Iwamori et al., 2007) suggested that: (i) an aqueous fluid released from the subducting oceanic crust forms a serpentinite + chlorite layer in the forearc mantle wedge just above the subducting slab and (ii) most of the H_2O is subducted to a depth where serpentine and chlorite in the serpentinite layer become unstable. This depth (up to 150 km) depends on the thermal structure of the slab, and is greater for older, colder plates. These results confirmed previous hypothesis (e.g., Tatsumi, 1989) that slab-derived water is not a direct trigger for the production of arc magmas and that a two-stage chemical–mechanical water transport process to the arc involves deep subduction of the hydrated forearc mantle. Kerrick and Connolly (2001) and Gorman et al. (2006) presented results from thermodynamic modeling of metamorphic devolatilization of subducted slab lithologies for pressures up to 6 GPa using an open system approach, which considers both fluid fractionation from source lithologies and infiltration from subjacent lithologies. In general, their models simulating pervasive fluid flow in subducting lithologies match the CO_2 fluxes measured from volcanic arcs more closely than models which assumed purely channelized flow (Gorman et al., 2006). Cagnioncle et al. (2007) investigated the distribution of hydrous fluid and subsequent melt in the mantle wedge using 2D models that included solid mantle flow with characteristic temperature distributions, aqueous fluid migration and mantle wedge melting. The results showed that solid mantle flow deflects hydrous fluids from their buoyant vertical migration through the wedge. In agreement with previous studied (e.g., Iwamori, 1998, 2000, 2004), melting does not occur directly above the region where hydrous fluids are released from the slab. Instead, a melting front develops where percolating hydrous fluids first encounter mantle material hot enough to melt.

Kimura et al. (2009) modeled geochemical characteristics of primitive magmas in intra-oceanic arcs based on the Arc Basalt Simulator (ABS), which combines thermo-mechanical subduction models and geochemical calculations. According to this computational approach variations in the magma geochemistry have been mainly attributed to the melting of depleted mantle wedge peridotite by the fluxing of fluids or melts derived from subducting oceanic crust. It has been further assumed that the difference in contributions from the subducted slab found among various arcs should be mostly controlled by the thermal structure of subduction zones. Based on these assumptions, the computational model of Kimura et al. (2009) predicts the partitioning of incompatible elements and Sr–Nd–Pb isotopic composition in slab-derived fluids and in arc basalt magmas generated by an open system fluid-fluxed melting of mantle wedge peridotite. In particular, the simulations predict a contrasting geochemical behavior between arcs along the Western and Eastern Pacific rims. Arc magmatism due to slab-derived fluids is proposed for the Western Pacific arcs, including the Kurile, NE Japan, and the Izu–Bonin–Mariana arcs. In contrast, slab melting better explains the origin of high-MgO intermediate lavas in the Eastern Pacific, although the role of slab fluids remains an important factor in some of the arcs.

Important challenges for modeling and understanding of geochemical and magmatic processes in subduction zones are related to the development of positively buoyant diapiric structures in the mantle wedge that originated from subducted rock mélanges (e.g., Behn et al., 2011; Castro and Gerya, 2008; Castro et al., 2010; Gerya and Yuen, 2003a; Hall and Kincaid, 2001; Marschall and Schumacher, 2012; Tamura, 1994; Tamura et al., 2011 and references

therein). In particular, island arc lavas, erupted above subduction zones, commonly contain a geochemical component derived from partial melting of subducted sediment (e.g., Behn et al., 2011 and references therein). Behn et al. (2011) found that the trace elements that form the sediment melt signature are retained in the sediments until the rocks have experienced temperatures exceeding 1050 °C, which are much higher than those at the surface of subducted slabs. Based on thermo-mechanical calculations, the authors suggested that subducted sediments detach from the downgoing slab at temperatures of 500–850 °C to form buoyantly rising diapirs, which undergo subsequent high-temperature melting inside the mantle wedge. Furthermore, subduction zones magmas show a characteristic range of compositions that reflect mixing in the magma source region between three components: hydrous fluids derived from the subducted oceanic crust, subducted sediments and peridotite mantle rocks. This variability can be explained by a two-step process (Marschall and Schumacher, 2012 and references therein): first, intensely mixed three-component (oceanic crust, sediments, serpentinites) subduction mélanges form along the slab interface; then, diapirs of low-density mélange material rise buoyantly from the surface of the subducting slab and transport the well-mixed mélange material into the hot subarc mantle. Based on combination of high-pressure melting experiments on rock mélanges and numerical thermo-mechanical models of subduction, it was proposed that melting of lithologically mixed diapiric structures in the mantle wedge can be responsible for relatively stable granodioritic composition and strongly variable time-dependent geochemical signatures of Cordilleran-type batholiths (Castro and Gerya, 2008; Castro et al., 2010). Recently, Vogt et al. (2013) tested these ideas by numerical modeling of geochemical variations caused by mechanical mixing in diapiric structures. They found that Sr and Nd isotopic ratios of the diapiric mélange vary as a function of time, depending on the changing proportions of the sedimentary and basaltic components. According to experimental constraints (Castro et al., 2010), partial melting of this mélange should produce melt with a relatively constant major element composition and time-dependent Sr and Nd isotopic ratios inherited from the mélange, thus closely matching relations observed in Cordilleran-type batholiths (Vogt et al., 2013).

None of the previous numerical subduction models directly incorporated geochemical transport processes into thermo-mechanical calculations. The main goal of this study is to perform such fully coupled geochemical–thermo-mechanical (GcTM) modeling in order to investigate Pb isotopic signatures of the two key "outputs" of subduction zones: (A) hydrated forearc mantle (including serpentinite mélanges) and (B) basaltic volcanics derived by fluid-fluxed mantle melting. In this study, we compare isotopic signatures for three different geodynamic regimes of intra-oceanic subduction systems (Baitsch-Ghirardello et al., 2014): (1) retreating subduction with backarc spreading, (2) stable subduction with high fluid-related weakening, and (3) stable subduction with low fluid-related weakening. The choice of Pb isotopes for our GcTM numerical modeling study is motivated by the fact that this incompatible element serves as one of the key geochemical tracers for subduction zones recycling and fluid processes (e.g., Deschamps et al. 2010; Ishizuka et al., 2003; Kimura et al., 2009; King et al., 2006, 2007; Kodolányi et al., 2012; Marschall and Schumacher, 2012; Ruepke et al., 2004; Scambelluri et al., 2004; Straub and Layne, 2003).

2. Numerical model description

Our computational model is based on the I2ELVIS code (Gerya and Yuen, 2003b, 2007) using conservative finite differences and a non-diffusive marker-in-cell technique to simulate multiphase flow. The thermo-mechanical model design and boundary conditions for our numerical experiments (Fig. 1) are identical to those of Baitsch-Ghirardello et al. (2014), who investigated different geodynamic regimes of intra-oceanic subduction. However, the GcTM model used in our study incorporates element partitioning between solid, fluid and melt and traces the isotopic evolution of the different components involved using fluid and rock markers. The physical properties of rocks used in our experiments are identical to those in Baitsch-Ghirardello et al. (2014) and are listed in Table S1 (supplement).

2.1. Boundary conditions

The 2D numerical model (Fig. 1) simulates intra-oceanic subduction system since its initiation at 0 Ma. The scaled size of the model is 300 km in depth and 4000 km in length with the subducting plate being about 2500 km long and the overriding plate is 1500 km (Fig. 2a). The rectangular non-uniform 2001x301-nodes grid contains a 1500 km long (from x = 1500 km to x = 3000 km, Fig. 1), high-resolution area (1 × 1 km) in the center of the model. The resolution is 5 × 1 km over the rest of the model. The oceanic crusts of both the subducting and the overriding plates represent an upper layer of hydrothermally altered basalts (2 km thick) overlying a 5 km thick layer of gabbro. The mantle consists of anhydrous peridotite. The initiation of subduction is prescribed by an initial rheologically weak zone with wet olivine rheology and low brittle/plastic strength ($\sin(\varphi) = 0.1$ where φ is the effective internal friction angle) in the mantle lithosphere with stronger rheology corresponding to dry olivine (Ranalli, 1995). A prescribed constant plate velocity is defined within the distant intra-plate region and drives the spontaneously bending oceanic slab.

The mechanical boundary conditions are free slip at the top and side boundaries, whereas the lower boundary is permeable in the vertical direction. The top surface of the lithosphere is treated as an internal free surface by using an 8–12.5 km thick top layer with low viscosity (10^{18} Pa s) and density (1 kg/m^3 for air above y = 10 km level, 1000 kg/m^3 for sea water below y = 10 km level). The large viscosity contrast caused by these low viscosity boundary layers minimizes shear stresses (<10^5 Pa) at the top of the lithosphere, making it an efficient free surface (e.g. Schmeling et al., 2008). In order to account for erosion and sedimentation processes at the plate surface, the following transport equation (Gorczyk et al., 2007) is solved at each time-step in Eulerian coordinates:

$$\partial y_{es}/\partial t = v_y - v_x \partial y_{es}/\partial x - v_s + v_e$$

where y_{es} is the vertical position of the surface as a function of the horizontal distance x; v_y and v_x are the vertical and horizontal components of the material velocity vector at the surface (y is positive downward, y = 0 at the top of the box); v_s and v_e are the sedimentation and erosion rates, respectively, as given in the following relations:

$v_s = 0$ mm/a $\quad v_e = 0.3$ mm/a for y<9 km
$v_s = 0.03$ mm/a $\quad v_e = 0$ mm/a for y>10 km

In regions with steep surfaces, for example in the trench, an increased erosion/sedimentation rate (1 mm/a) is implemented to account for additional mass transport.

2.2. Hydration process

The equilibrium mineralogical water content is computed for each lithology as a function of pressure and temperature (Fig. 2a–c) from thermodynamic data by free energy minimization (Connolly, 2005; Gerya et al., 2006). In addition, water may be present as a pore fluid with concentrations of up to 2 wt.% in sediments and hydrothermally altered basalt. The pore water content $X_{H2O(P)}$ (wt.%) decreases linearly

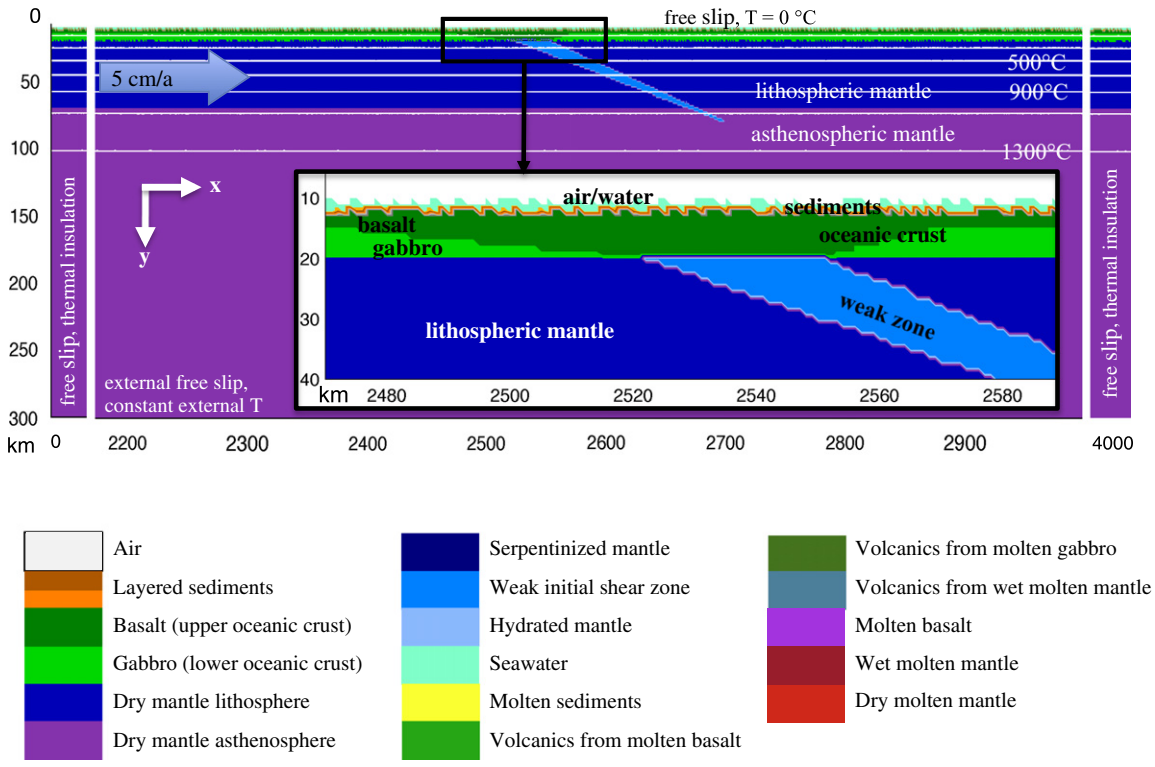

Fig. 1. Numerical model setup. Prescribed subducting plate velocity (blue arrow) remains constant during the entire experiment. Isotherms (white lines) from 100 °C with 200 °C intervals. Material colors are shown for all figures. Two layers in the sediments have the same material properties but are differently colored to better visualize deformation. Same concerns dry mantle lithosphere and asthenosphere. (For interpretation of the references to color in this figure legend, the reader is referred to the web version of this article.)

from the maximal value of $X_{H2O(P0)}$ =2 wt.% at the surface to 0 wt.% at 75 km depth:

$$X_{H2O(P)} = (1–0.013 \cdot \Delta y) \cdot X_{H2O(Po)},$$

where Δy is depth (0–75 km). The water release also mimics the effects of low-temperature (T < 573 K) reactions, which are not included in our thermodynamic database.

The slab dehydrates as it sinks. The timing of H_2O release by dehydration reactions is determined by the physicochemical conditions of the model (Fig. 2a–c) and the assumption of thermodynamic equilibrium. Fluids propagate upward into the mantle wedge. Seismic data on natural cases suggest that up to 2 wt.% of water is absorbed (Bostock et al., 2002; Carlson and Miller, 2003). Water propagation is modeled in the form of water markers: dehydration reactions lead to a release of water, the amount of which is stored in a newly generated water marker. Water markers move through the rocks with the following velocity:

$$v_{x(water)} = v_x, \quad v_{y(water)} = v_y - v_{y(percolation)}$$

v_x and v_y describe the local velocity of the mantle and $v_{y(percolation)}$ indicates the relative velocity of upward percolation ($v_{y(percolation)}$ = 10 cm/a in our experiments). Water is released by the marker as soon as it encounters a rock capable of absorbing water by hydration or melting reactions at given PT-conditions and rock composition (Gorczyk et al., 2007; Nikolaeva et al., 2008; Sizova et al., 2010).

2.3. Partial melting and melt extraction

Because the H_2O transport model does not permit complete hydration of the peridotic mantle, the mantle solidus is intermediate between the wet and dry peridotite solidi. To account for this behavior, we assume that the degree of both hydrous and dry melting is a linear function of pressure and temperature (e.g. Gerya and Yuen, 2003a). In this model the standard (i.e. without melt extraction) volumetric degree of melting M_0 is,

$$M_0 = 0 \quad \text{when } T<T_{solidus}, M_0 = (T-T_{solidus})/\left(T_{liquidus}-T_{solidus}\right)$$
$$\text{when } T_{solidus}<T<T_{liquidus}, M_0 = 0 \quad \text{when } T>T_{liquidus},$$

where $T_{solidus}$ is the solidus temperature (wet and dry solidi are used for the hydrated and dry mantle, respectively) and $T_{liquidus}$ is the dry liquidus temperature at a given pressure and rock composition (Table S1, supplement). To simulate melt extraction from partially molten rocks (e.g. Nikolaeva et al., 2008; Sizova et al., 2010) we define a melt extraction threshold M_{max} = 4% and a non-extractable amount of melt M_{min} = 2% that remains in the source.

The amount of melt extracted during each experiment is tracked by rock markers. The total amount of melt, M, for every marker takes into account the amount of previously extracted melt and is calculated as

$$M = M_0 - \Sigma_n M_{ext}$$

where $\Sigma_n M_{ext}$ is the total melt fraction extracted during the previous n extraction episodes. In our models, the rock is considered non-molten (refractory), when the extracted melt fraction is bigger than the standard one (i.e. when $\Sigma_n M_{ext} > M_0$). If the total amount of melt M exceeds the threshold M_{max}, the melt fraction $M_{ext} = M - M_{min}$ is extracted and $\Sigma_n M_{ext}$ is updated. The extracted melt fraction M_{ext} is assumed to propagate upward much faster than the convective motion of the mantle. At the surface, all extracted markers build up a new volcanic arc crust and thereby retain their volume and composition (Nikolaeva et al., 2008).

2.3.1. Rheological model

The effective stress- and temperature-dependent creep viscosity of rocks is computed according to experimentally determined flow laws (Ranalli, 1995) (Table S1, supplement). Fluid and melt migration affects

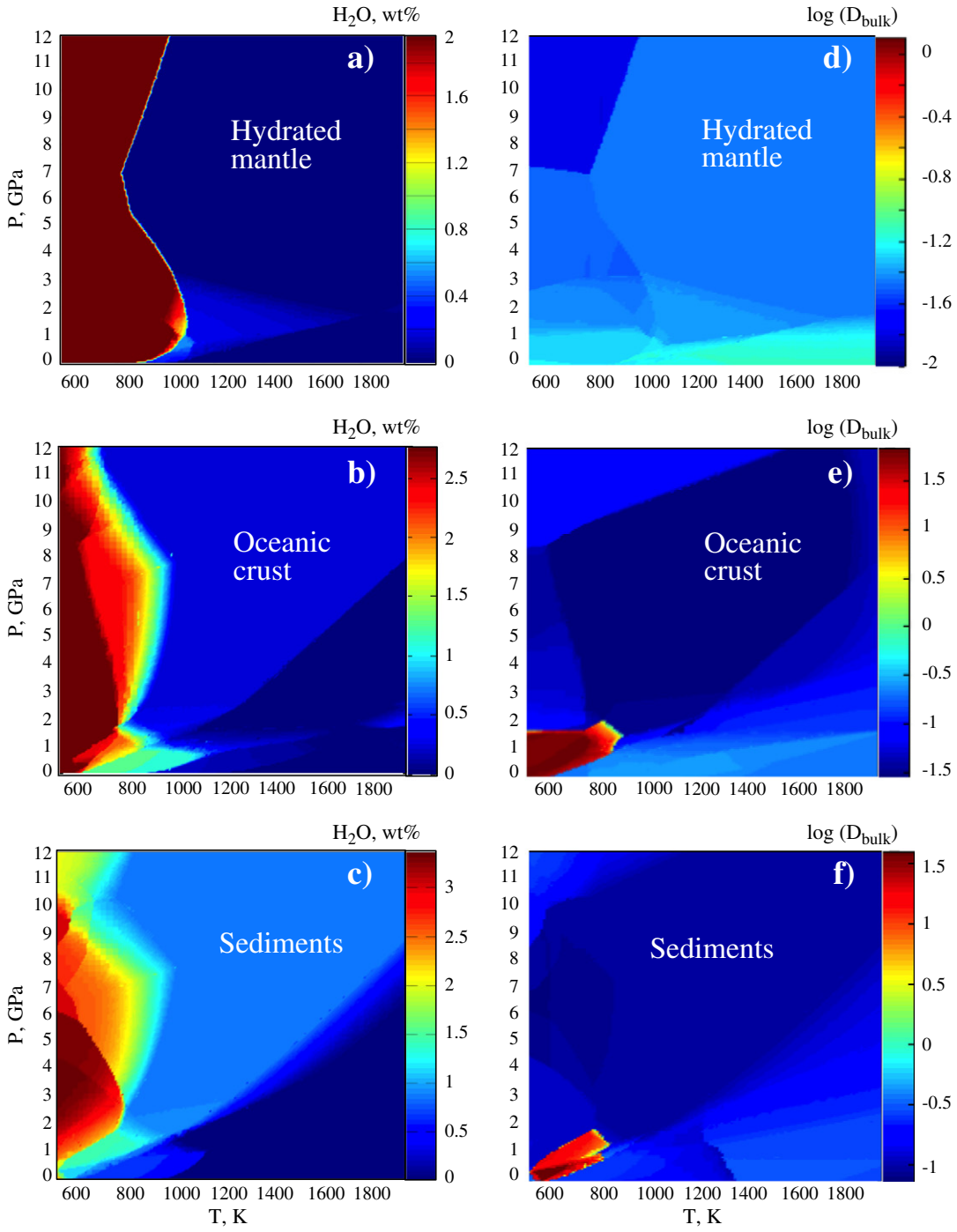

Fig. 2. Equilibrium water content (a)–(c) and rock/fluid Pb partition coefficient D_{bulk} (d)–(f) computed from thermodynamic data and rock compositions (Gerya et al., 2006) using Gibbs energy minimization (Connolly, 2005). Note that maximal water content in rocks is limited to account for incomplete and heterogeneous hydration (Gerya et al., 2006): sediments = 7.60 wt.%; oceanic crust = 2.78 wt.%; hydrated mantle = 1.98 wt.%. Detailed phase diagrams are presented in Fig. S2–S4 (supplement).

the brittle/plastic strength of rocks. In our model, the effects are simulated by the Drucker–Prager yield criterion as follows:

$$\sigma_{yield} = c + P_{solid}\sin(\varphi),$$
$$\sin(\varphi) = \lambda_{fluid}\ \sin\left(\varphi_{dry}\right) \text{ and } \lambda_{fluid}$$
$$= 1 - P_{fluid}/P_{solid} \text{ in the regions of fluid percolation, } \sin(\varphi)$$
$$= \lambda_{melt}\ \sin\left(\varphi_{dry}\right) \text{ and } \lambda_{melt}$$
$$= 1 - P_{melt}/P_{solid} \text{ in the regions of melt percolation.}$$

Thus, the local brittle/plastic yield strength σ_{yield} of a rock depends on (1) the mean stress (pressure) P_{solid} on the solid, (2) the cohesion, c, which is the strength at $P_{solid} = 0$, and (3) the effective internal friction angle, φ, which is calculated from the friction angle of dry rocks, φ_{dry} (for values of c and sin (φ_{dry}) see Table S1, supplement), and the pore fluid/melt pressure factors $\lambda_{fluid}/\lambda_{melt}$. According to our model, the pore fluid pressure P_{fluid} reduces the yield strength of rocks subjected to percolation of water markers released from the slab. Similarly, ascending extracted melts reduce the yield strength in the column of rock between the source of the melt and the surface. λ_{fluid} and λ_{melt} factors are varied in different numerical experiments

Table 1
Initial values for Pb isotopes for three "input" lithologies used in numerical experiments.

Rock type	Pb [ppm]	Pb isotopes [10^{-9} mol/kg]		References
Sediments	20.2	^{204}Pb	1310	GLOSS
		^{206}Pb	24,700	Plank and Langmuir (1998)
		^{207}Pb	20,500	
		^{208}Pb	50,800	
Oceanic crust (basalts, gabbro)	0.577	^{204}Pb	38.5	MORB
		^{206}Pb	702	Arevalo and McDonough (2010)
		^{207}Pb	594	
		^{208}Pb	1450	
Mantle (dry peridotite)	0.0235	^{204}Pb	1.52	DM
		^{206}Pb	28.6	Salters and Stracke (2004)
		^{207}Pb	24.3	
		^{208}Pb	59.1	

(Fig. S1, Supplement) corresponding to different geodynamic regimes of subduction (Baitsch-Ghirardello et al., 2014; Gerya and Meilick, 2011).

2.4. Geochemical model: implementation of geochemical equations and parameters

In our simplified GcTM model we account only for three isotopically distinct initial "input" lithologies (Table 1): sediments (GLOSS, Plank and Langmuir, 1998), altered oceanic crust with basalt and gabbro (MORB, Arevalo and McDonough, 2010) and depleted dry mantle (DM, Salters and Stracke, 2004). The initial Pb content and isotopic composition for each lithology are implemented in the corresponding rock markers at the beginning of each experiment. The radioactive decay is not taken into account in our study due to the relatively short timescales (0–25 Ma) involved into the numerical simulations, in which radioactive decay of U and Th has a negligible effect on the Pb isotope ratios.

We assume that partitioning of trace elements between the solid and fluid phases is defined by Rayleigh distillation during slab dehydration, in which case the trace element concentrations (C) are:

$$C_{fluid} = \frac{C_0}{D_{bulk}}(1-F)^{\frac{1}{D_{bulk}}-1},$$

$$C_{solid} = \frac{C_0 - C_{fluid} * F}{1-F},$$

where

$$D_{bulk} = \sum_{1}^{n} X_a * D_a,$$

and D_a is the mineral/fluid partition coefficient (Table 2, and Fig. 2), X_a is the mass fraction of a mineral i in the rock, F is the fluid fraction, and C_0 is the concentration of element in the rock before the fluid release. Subsequent hydration of the mantle wedge rocks changes rock and fluid compositions as well. This hydration process is modeled as one of dissolving anhydrous minerals by a fluid and subsequent recrystallization of the hydrous assemblage. The resulting trace element concentrations are (Albarède, 2003):

$$C_{fluid} = C_0 * (1-F)^{D_{bulk}-1},$$

$$C_{solid} = C_0 * D_{bulk} * (1-F)^{D-1} * F + C_{0\_solid}(1-F),$$

where C_{0_solid} is the element concentration in the rock before hydration. The stable mineralogy for each lithology as a function of pressure and temperature (Fig. 2) is computed from thermodynamic data by free energy minimization (Connolly, 2005; Gerya et al., 2006). For simplicity the partition coefficients are assumed to be independent of pressure and temperature (see Kessel et al., 2005). Similarly, trace elements are redistributed between rocks and melt phase when partial melting takes place. We assume that melt and host rocks are in equilibrium before melt extraction (Ayers, 1998):

$$C_{melt} = \frac{C_0}{F_{total} + D_{bulk} - F_{total} * D_{bulk}},$$

$$C_{solid} = \frac{C_0 - C_{melt} * F_{extracted}}{1-F_{extracted}},$$

where C is concentration of element in melt or solid, D_{bulk} is rock/melt partition coefficient of element, C_0 is concentration of element in the system before the melt extraction, F_{total} is fraction of melt produced, $F_{extracted}$ is fraction of melt extracted to the surface ($F_{total} - F_{residual}$). The composition of magmatic arc rocks is defined by the composition of extracted melts; effects such as the decay of uranium and thorium during melt percolation towards the surface are ignored, which maximizes the geochemical signals originating from trace element partitioning during dehydration/hydration and melting. This assumption is supported by short times for source-to-surface melt migration indicated by ^{226}Ra–^{230}Th systematics (Turner et al., 2001).

Fig. 2 shows the results of our calculations of equilibrium mineralogical water content (Fig. 2a–c) and bulk partitioning coefficients (Fig. 2d–f) for three key lithologies. Correlation between the equilibrium water

Table 2
Partition coefficients of Pb between different minerals and fluid/melt phase used in the numerical experiments.

Mineral	$D_{mineral/fluid}$	$D_{mineral/melt}$	Comments
Albite	0.36[a]	0.425[f]	
Amphibole	0.1[a]	0.07[b]	
Antigorite	0.1[a]	–	Antigorite does not coexist with melt.
Biotite	0.89[f]	0.89[f]	
Chlorite	0.1[a]	–	Chlorite does not coexist with melt.
Clinozoisite	204.5[i]	204.5[i]	$D_{mineral/melt} = D_{mineral/fluid}$ is assumed.
Cordierite	0.03[m]	–	Cordierite does not coexist with melt.
Feldspar	0.36[a]	0.425[f]	
Garnet	0.0005[a]	0.018[b]	
Ilmenite	0.75[f]	0.75[f]	$D_{mineral/melt} = D_{mineral/fluid}$ is assumed.
K-feldspar	0.36[a]	0.425[f]	
Lawsonite	0.1[a]	0.1[a]	$D_{mineral/melt} = D_{mineral/fluid}$ is assumed.
Mica (phlogopite)	0.0925[b]	0.089[b]	
Na-amphibole	0.89[f]	–	Na-amphibole does not coexist with melt.
Olivine	0.0001[a]	0.0004[o]	
Omphacite	0.0013[a]	0.01[o]	
Orthopyroxene	0.0001[b]	0.0013[o]	
Rutile	0.0154[q]	0.0154[q]	
Sphene	0.525[x]	0.525[x]	$D_{mineral/melt} = D_{mineral/fluid}$ is assumed.
Spinel	0.0005[c]	0.00005[o]	
Talc	0.1[a]	–	Talc does not coexist with melt.
Zoisite	8.6[n]	8.6[n]	$D_{mineral/melt} = D_{mineral/fluid}$ is assumed.

The Kds are taken from: a = McKenzie and O'Nions (1991); b = Adam & Green (2006); c = Elkins et al. (2008); f = Ewart & Griffin (1994); i = Zack et al. (1997 2002); m = Bea et al. (1994); n = Klimm et al. (2008); o = Hawkesworth et al. (1993); q = Foley et al. (2000), Foley & Jenner (2004); x = Klemme et al. (2005).

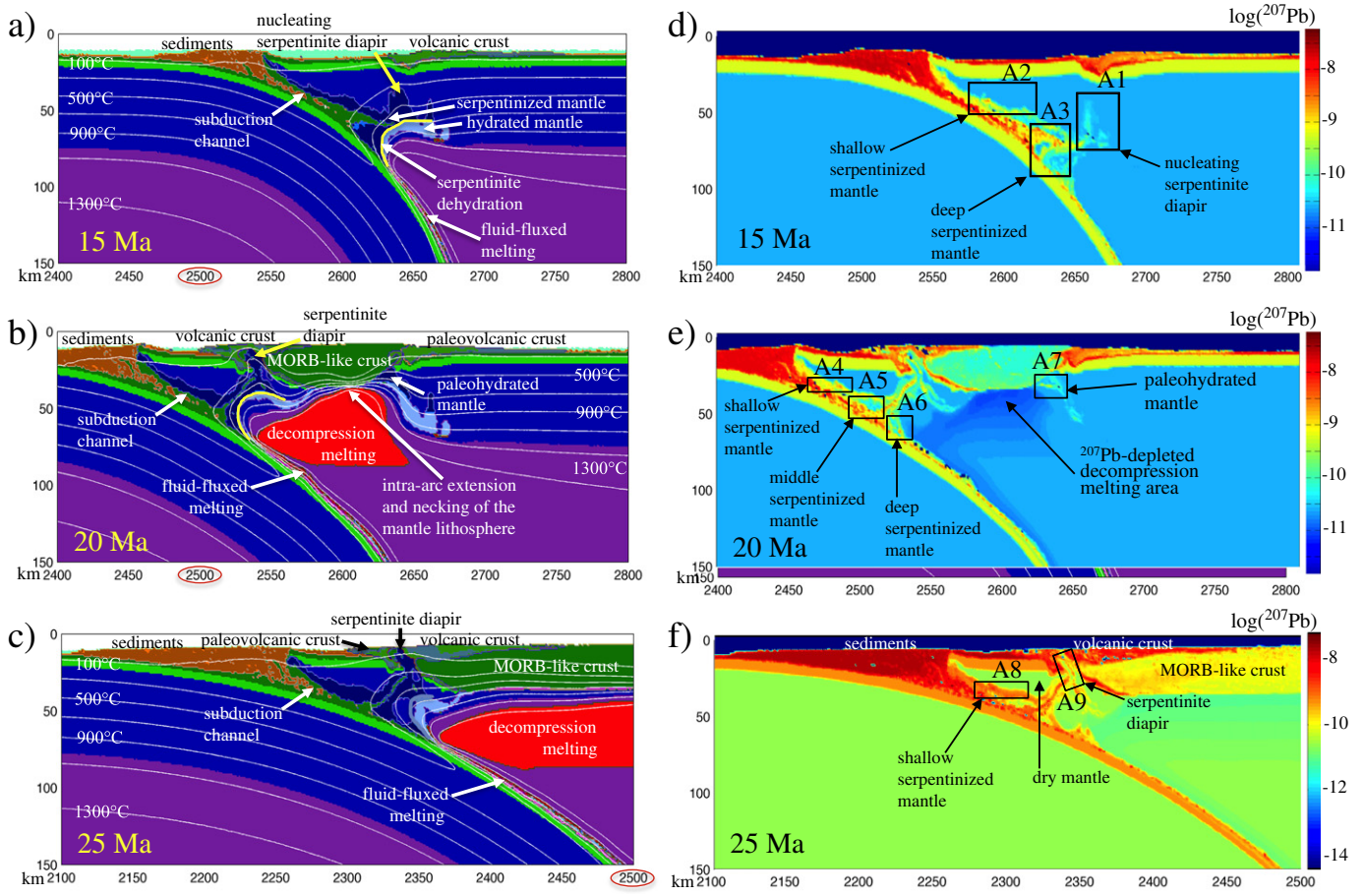

Fig. 3. Reference model for the retreating subduction regime; ($\lambda_{fluid} = 0.02$ and $\lambda_{melt} = 0.01$, model bet23B in Fig. S1, supplement). (a)–(c) Evolution of the lithological field (colors, cf. Fig. 1) and isotherms (white lines, from 100 °C with 200 °C intervals). (d)–(f) Evolution of ^{207}Pb concentrations, black labeled rectangles A1–A9 mark hydrated mantle sampling areas for which isotopic ratios are shown in Fig. 4. Yellow lines in (a)–(c) show serpentinite dehydration. Time is shown since the beginning of convergence. Note that colorscale of (f) has been changed to highlight differences between the serpentinized and dry mantle lithosphere. (For interpretation of the references to color in this figure legend, the reader is referred to the web version of this article.)

content in rocks and the computed bulk Pb partition coefficient results from the fact that the trace element partition coefficients of hydrous minerals are much different than those of nominally anhydrous minerals (Table 2). In our models the partition coefficient (D_{bulk}) of Pb in basalt and sediments is mainly controlled by clinozoisite (red colored region in Fig. 2e and f), which is an important carrier for Pb and other elements such as Sr, Th and U in the subduction zone close to the slab–mantle interface (Zack, 2002). Therefore $D_{clinozoisite/fluid}$ is an important value for modeling trace element composition of fluids released by dehydration process of subducting oceanic crust (Schmidt and Poli, 1998; Zack, 2002). Some mineral/melt partition coefficients are unknown. In such cases we adopted the value reported for the corresponding mineral/fluid partition coefficient (Table 2).

3. Results

In this GcTM numerical modeling study we investigated Pb isotopes evolution for three geodynamic regimes of intra-oceanic subduction found in our previous numerical experiments (Baitsch-Ghirardello et al., 2014) as a function of fluid and melt-induced rheological weakening effects (Fig. S1, supplement): (1) retreating subduction with backarc spreading, (2) stable subduction with high fluid-related weakening, and (3) stable subduction with low fluid-related weakening. A short description of these regimes is given below; more details are presented by Baitsch-Ghirardello et al. (2014). We found, that these three regimes reveal significant differences in Pb isotopes behavior, which is described below on the basis of three reference models (cf. models bet23B, bet51, bet15 in Fig. S1, supplement).

3.1. Retreating subduction with backarc spreading

The retreating subduction regime occurs in experiments with strong weakening of the overriding plate by both fluids and melts (λ_{fluid} =0.001–0.0333, λ_{melt} = 0.001–0.05) (Fig. S1, supplement). In the reference model bet23B with $\lambda_{fluid} = 0.02$, $\lambda_{melt} = 0.01$ (Fig. 3) the magmatic arc starts growing 5 to 6 Ma after subduction initiation. The volcanic crust is produced from the molten hydrated peridotite of the mantle wedge and from a small amount of molten basalt and gabbro of the subducted plate (Fig. 3a). Extension in the fore/intra-arc region starts at 15–20 Ma (Fig. 3b) as the result of rheological weakening of the overriding plate by hydration/serpentinization processes and melt propagation. Lowered viscosity of serpentinized forearc mantle (dark blue area in Fig. 3a,b) together with melt-induced weakening of the arc lithosphere ($\lambda_{melt} = 0.01$) triggers necking of the overriding plate above the upper-left corner of the asthenospheric mantle wedge (long arrow in Fig. 3b), which in turn triggers decompression melting in the mantle wedge, and initiate an intra-arc extension associated with MORB-like crust formation atop the lithospheric necking area

(Fig. 3b). Parallel to the development of intra-arc extension and decompression melting hydration of the mantle above the slab extends laterally (light blue color in Fig. 3b) triggered by a rising hot partially molten asthenospheric mantle wedge corner (Fig. 3b). Above this corner, the diapir of serpentinite moves upward through the overriding plate and emplaces into the lower crust (Fig. 3b). As a consequence of necking of the overriding plate, the trench starts to retreat (cf. changing coordinates in the bottom of Fig. 3b and c). Decompression melting continues to generate a new crust with MORB-like composition inside the widening oceanic backarc basin, which splits the original arc into the frontal and rear parts (Fig. 3b and c). The frontal arc remains active and migrates together with the trench (Fig. 3b and c). The rear arc gradually becomes an extinct paleo-magmatic arc composed of subduction-related paleovolcanic crust (Fig. 3b) behind the back arc basin. It remains active until ca. 25 Ma has been fueled by melting of previously hydrated subarc lithosphere. During the progress of extension and trench retreat, hot asthenosphere rises along the slab, thus causing an increase in the slab surface temperature at shallower depths (cf. positions of yellow serpentinite dehydration curves in Fig. 3a–c). As the result, dehydration of the slab starts earlier and serpentinized forearc mantle extent (60 km depth) become shallower compared to the initial stages of subduction (80 km depth, cf. Fig. 3 a–c). After 25 Ma, exhumation of the serpentinized diapir composed of subduction mélange rocks (Fig. 3c) cuts the active frontal arc in two parts: magmatically inactive frontal paleoarc and active middle arc (Fig. 3c).

3.1.1. Pb isotopes in the mantle wedge

After 15 Ma of model development wide serpentinite area (dark blue color in Fig. 3a) underlain by the hydrated serpentine-free mantle (light blue color in Fig. 3a) has formed in the forearc region of the subduction zone. Within this area, an uprising progressively serpentinized zone (nucleating serpentinite diapir, Fig. 3a) developing away from the slab has a mixed *binary* Pb isotope signature between mantle peridotite and MORB without any significant involvement of sediments (Figs. 3a,d, 4a). In contrast, the serpentinized forearc mantle of subduction channel mélange formed atop the slab surface shows a pronounced sediment influence (Figs. 3a,d and 4b,c). The degree of isotopic heterogeneity increases with depth. At shallow depths, *double binary* MORB–mantle and mantle–sediments signatures are prevalent (Fig. 4b) as the result of *incipient* mantle serpentinization by fluids coming from two distinct crustal sources. In contrast, at lager depths strongly mixed *triple* mantle–MORB–sediments signatures become clearly dominant (Fig. 4c) as the result of mechanical mixing and multiple hydration/dehydration cycles inside the deep subduction channel mélange. In particular, fluids produced by dehydration of serpentinites subducted atop the slab to asthenospheric depths (see transition between serpentinized and serpentine-free hydrated mantle in Fig. 4a) percolate upward and change isotopic signatures of mechanically mixed crustal and mantle rocks in the serpentinite mélange located in the bottom of the subduction channel.

At 20 Ma, the decompression melting area shows a depleted signature of ^{207}Pb (cf. Fig. 3b and e), which decreases with depth. The serpentinites of subduction channel exhibit a heterogeneous Pb isotope signature, depending on the origin of fluids and the intensity of mantle hydration (Figs. 3b,e and 4d–f). The degree of isotopic heterogeneity again increases with depth: *double binary* MORB–mantle and mantle–sediment trends are found in shallow channel serpentinites (Fig. 4d) whereas *triple* MORB–sediment–mantle mixing occurs in the middle and deep channel serpentinites (Fig. 4e,f). On the other hand, paleohydrated serpentinized mantle located away from the slab under the rear arc (Figs. 3b,e and 4g) preserves simple *binary* MORB–mantle isotopic signature formed at the earlier stages of subduction (cf. Fig. 4a and g).

After 25 Ma, the Pb isotope signature in the exhumed serpentinite diapir is rather similar to *triple* MORB–sediment–mantle signatures of deep subduction channel mélange (cf. Fig. 4i and c,f). In contrast, *double*

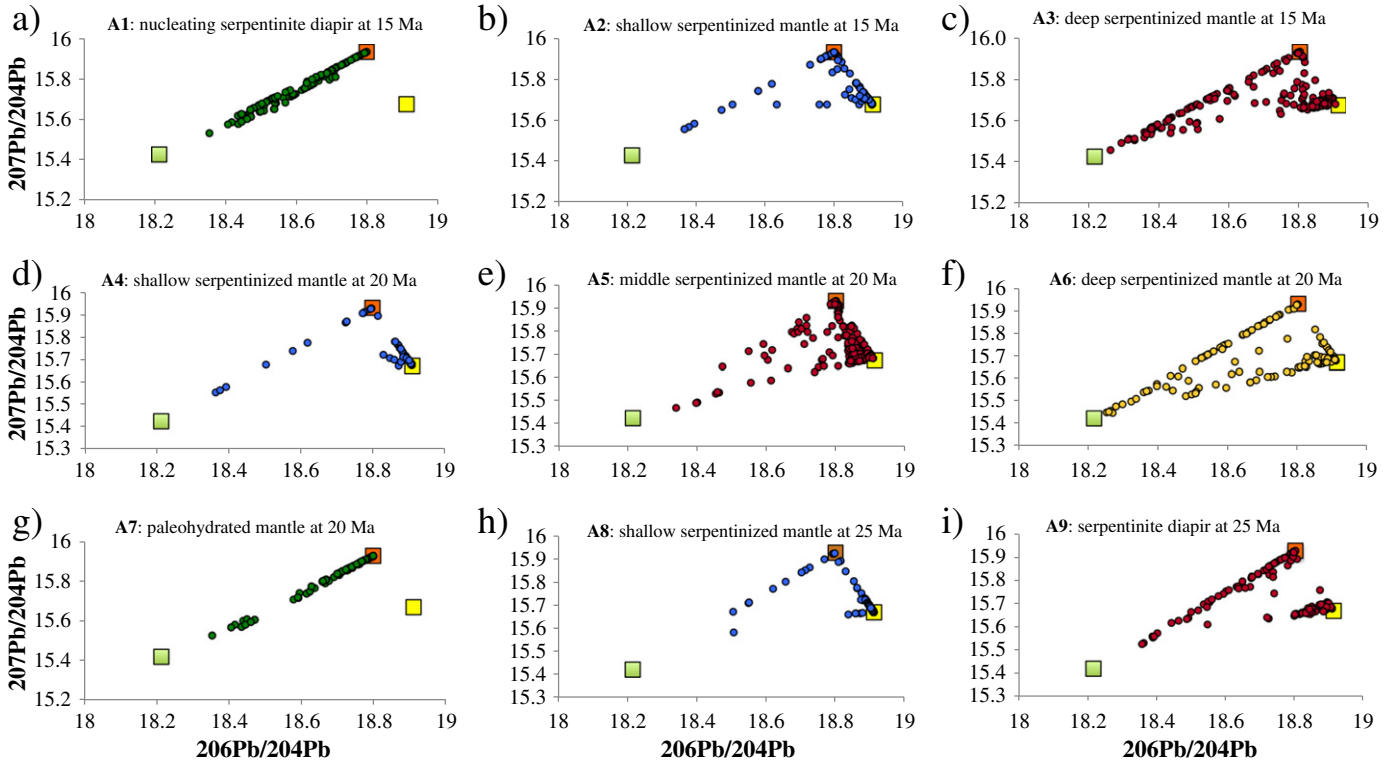

Fig. 4. Evolution of ^{207}Pb/^{204}Pb and ^{206}Pb/^{204}Pb isotopic ratios in various regions of the hydrated/serpentinized mantle during retreating subduction. Sampling areas A1–A9 are shown in Fig. 3d–f. Solid rectangles correspond to three initial ("input") lithologies (Table 1): sediments (yellow), oceanic crust (green) and depleted dry mantle (orange). (For interpretation of the references to color in this figure legend, the reader is referred to the web version of this article.)

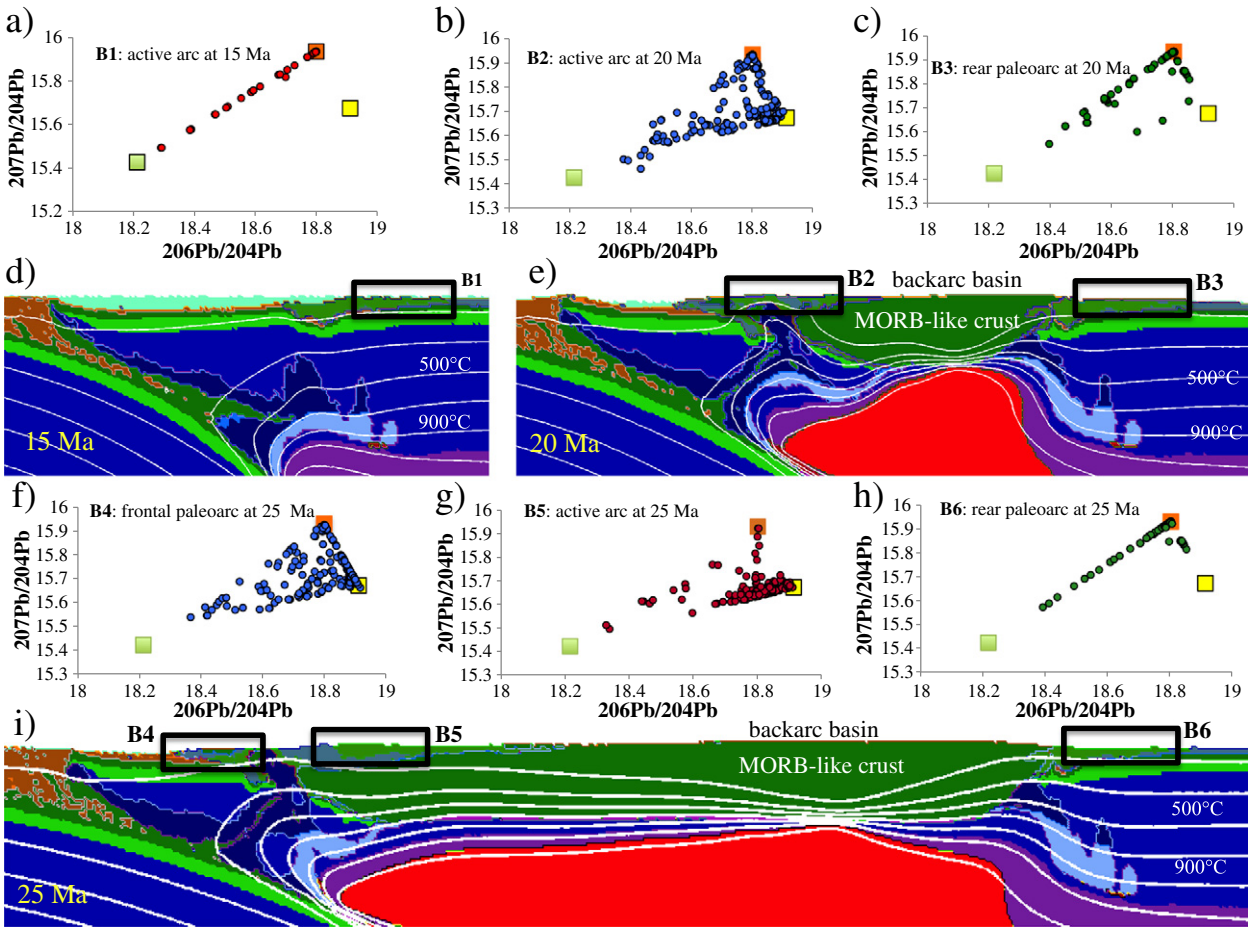

Fig. 5. Evolution of $^{207}Pb/^{204}Pb$ and $^{206}Pb/^{204}Pb$ isotopic ratios in basaltic crust (a)–(c), (g)–(h) derived by fluid-fluxed mantle melting at different stages of retreating subduction (d), (e), and (i). Sampling areas of the crust B1–B6 are shown by black rectangles in (d), (e), and (i). Solid rectangles correspond to three initial ("input") lithologies (Table 1): sediments (yellow), oceanic crust (green) and depleted dry mantle (orange). Colors for (d), (e), and (i) are as in Fig. 1; isotherms (white lines) are shown from 100 °C with 200 °C intervals; time is shown since the beginning of convergence. (For interpretation of the references to color in this figure legend, the reader is referred to the web version of this article.)

binary MORB–mantle and sediments–mantle signatures are still prevalent in the shallower portions of the subduction channel (Fig. 4h).

3.1.2. Pb isotopes in magmatic products of fluid-fluxed mantle melting

During the first 15 Ma of oceanic crust subduction and dehydration the magmatic arc is fueled by fluid-fluxed mantle melting (at 80 to 150 km depth) and a small amount of basaltic crust melting is also observed atop the slab. At this immature subduction stage, no significant amount of sediments is yet subducted and dehydrated at depths (Fig. 3a). Consequently, the Pb isotope ratios in the arc volcanics are dominated by the *binary* trend between the depleted mantle and MORB (Fig. 5a,d).

After 20 Ma of model development, subduction channel mélange formation associated with deep subduction and dehydration of sediments notably changes geochemical signatures in the mantle-derived magmas of the active frontal arc (Fig. 5b,e). This arc shows dominance of the *triple* MORB–sediment–mantle geochemical mixing trend (Fig. 5e). At the same time, magmatic products of deactivating rear paleoarc preserve earlier dominantly *binary* MORB–mantle trend with negligible sedimentary signal (Fig. 5c,e).

At 25 Ma, the frontal arc become split by the serpentinite diapir into inactive frontal paleoarc and active middle arc (Figs. 3c,5i). The geochemical contrast between the frontal paleoarc and the rear paleoarc remains preserved from the previous stages of subduction (cf. Fig. 5f and h, b and c). On the other hand, due to the growth of large accretionary prism, the amount of subducted sediments and sediments-polluted serpentinites (e.g., Fig. 4f) increases, which is reflected by the dominance of sedimentary fluid signatures along the *binary* MORB–sediment trend in volcanics of the active middle arc at 25 Ma (cf. Fig. 5g, and b).

3.2. Stable subduction with high fluid-related weakening

The stable subduction regime with high fluid-related weakening occurs in experiments with strong weakening of the forearc mantle by fluids ($\lambda_{fluid} \leq 0.001$) and lowered weakening of the subarc mantle by melts ($\lambda_{melt} \geq 0.05$) (Fig. S1, supplement). Increased strength of the subarc mantle caused by the reduced melt-related weakening precludes overriding plate necking (Baitsch-Ghirardello et al., 2014) and thus no intra-arc extension with decompression melting is produced (cf. Figs. 6 and 3). Consequently, stable subduction develops single magmatic arc with no backarc basin. In the reference model bet51 with $\lambda_{fluid} = 0.001$ and $\lambda_{melt} = 0.05$ (Fig. 6) the magmatic arc starts growing 5 to 8 Ma after subduction initiation. The arc is mainly fueled by fluid-fluxed melting of forearc mantle and oceanic crust subducted atop the slab (Fig. 6b). Volcanics derived from molten gabbro and sediments are rare. This stable subduction regime develops a wide serpentinized subduction channel mélange in the forearc mantle, in which the subducted basaltic crust is mechanically mixed with the serpentinized forearc mantle (Fig. 6b,c). Intense mixing is promoted by an increased degree of fluid-related weakening that reduces the effective viscosity of the mélange (Gerya et al., 2002). Two narrow

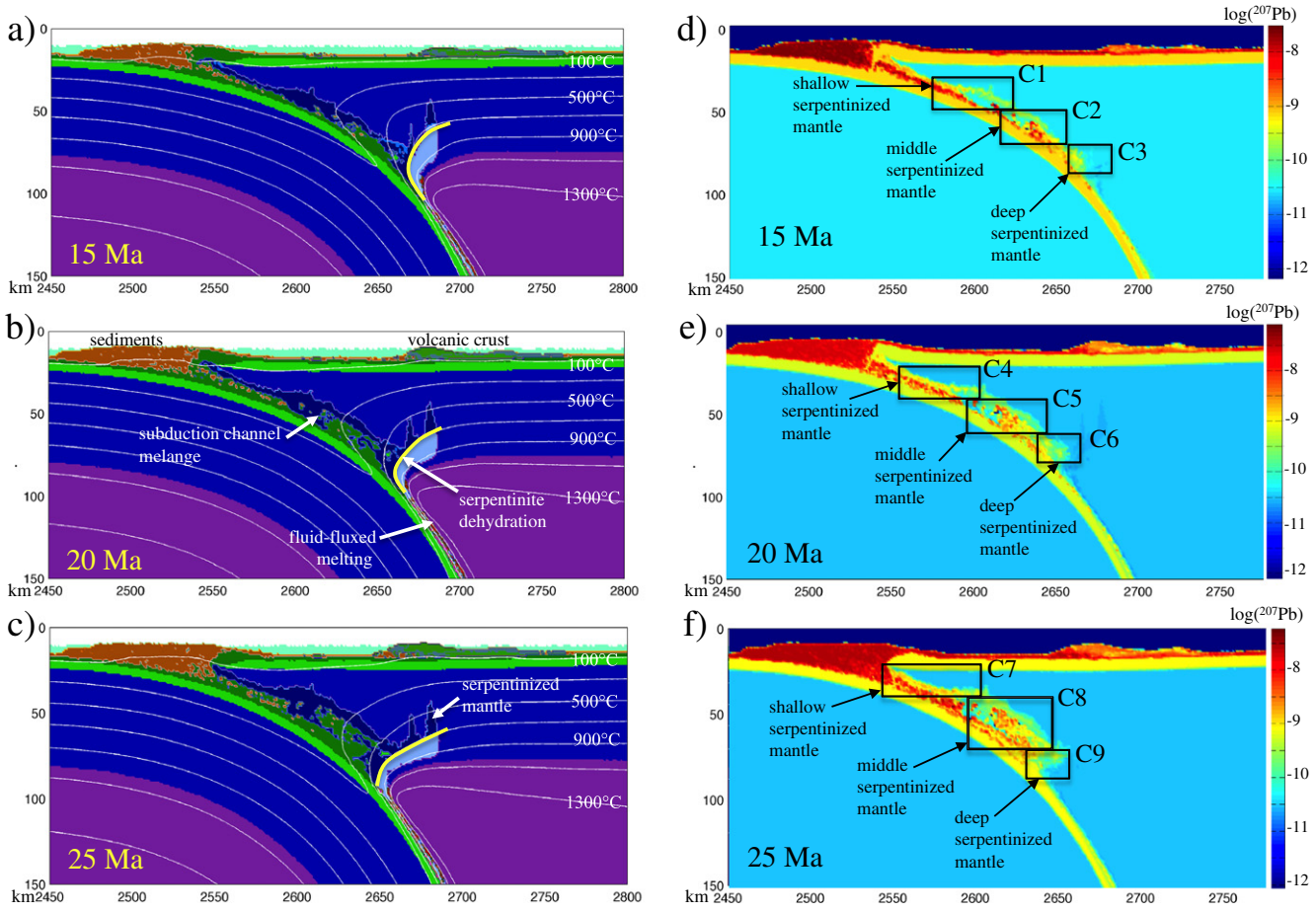

Fig. 6. Reference model for the stable subduction regime with high fluid-related weakening; ($\lambda_{fluid} = 0.001$ and $\lambda_{melt} = 0.05$, model bet51 in Fig. S1, supplement). (a)–(c) Evolution of the lithological field (colors, cf. Fig. 1) and isotherms (white lines, from 100 °C with 200 °C intervals). (d)–(f) Evolution of ^{207}Pb concentrations, black labeled rectangles C1–C9 mark hydrated mantle sampling areas for which isotopic ratios are shown in Fig. 7. Yellow lines in (a)–(c) show serpentinite dehydration. Time is shown since the beginning of convergence. (For interpretation of the references to color in this figure legend, the reader is referred to the web version of this article.)

vertical zones of mantle serpentinization develop in the subarc mantle lithosphere away from the slab (spike-like dark blue areas in Fig. 6b), however no serpentinite diapirs nucleate from these zones at the later stage (cf. Figs. 3c and 6c).

3.2.1. Pb isotopes in the mantle wedge

After 15 Ma of model development the shallow, middle and deep serpentinized forearc mantle exhibits a moderate Pb isotope heterogeneity in the relatively narrow serpentinized area formed atop the slab (cf. Fig. 6a and c). The progressively serpentinized zone has a mixed Pb isotope signature between mantle peridotite, MORB and sediments. Similarly to the extensional model, Pb isotope ratios in the shallow and middle forearc mantle typically show *double binary* mantle–MORB and mantle–sediment trends (Fig. 7a,b), whereas deep forearc mantle reveals *double binary* mantle–MORB and MORB–sediment trends (Fig. 7c).

After 20–25 Ma of subduction, the serpentinites of broadening subduction channel continue to exhibit a heterogeneous Pb isotope signature, depending on the origin of the fluids and the intensity of mantle hydration (Fig. 6e,f). The degree of isotopic heterogeneity increases with depth. Shallow and middle forearc mantle show dominance of the same *double binary* mantle–MORB and MORB–sediment trends as before (Fig. 7d,e and g,h), whereas in the deep forearc mantle the earlier *double binary* trends disappears in favor to a broad dispersion between all three signatures (mantle, MORB and sediments, Fig. 7f,i) which are similar to the triple geochemical mixing trend of the deep serpentinite mélange found in extensional subduction models (Fig. 4c, f). Sedimentary influence in the deep serpentinite melange clearly increases with time (cf. Figs. 7c,f,i) so that MORB–sediments isotopic mixing trend become dominant at 25 Ma (Figs. 7i).

3.2.2. Pb isotopes in magmatic products of fluid-fluxed mantle melting

At 25 Ma, we investigate the distribution of Pb isotopes in the stratified arc volcanics derived from hydrated partially molten peridotite within the time period of 15–25 Ma (Fig. 8). The analyzed volcanics is mainly produced by fluid-fluxed mantle melting and melting of basaltic crust subducted atop the slab (Fig. 8a,b). Concentration of ^{206}Pb in this volcanics is notably increased at the trenchward side of the magmatic arc (dark red area in Fig. 8b). Isotopic ratios in fluid-fluxed melting products show *triple* MORB–mantle–sediment mixture for the earliest volcanic crust formed at 15–17 Ma of model development (Fig. 8c). At the later stage (17–24 Ma), *binary* MORB–mantle trend without significant addition of sediments becomes dominant (Fig. 8d,e), which is in strong contrast with sediment-rich geochemistry of late magmatic products in the extensional arc (Fig. 5c,g). On the other hand, similar binary signatures are characteristic for the earliest pre-extension stages (3–15 Ma) of extensional subduction model (Fig. 5a).

3.3. Stable subduction with low fluid-related weakening

The stable subduction regime with low fluid-related weakening (Fig. 9) occurs in experiments with reduced weakening of the forearc mantle by fluids ($\lambda_{fluid} \geq 0.0333$) irrespective of melt-induced weakening (Fig. S1, supplement). In these models stable trench position is

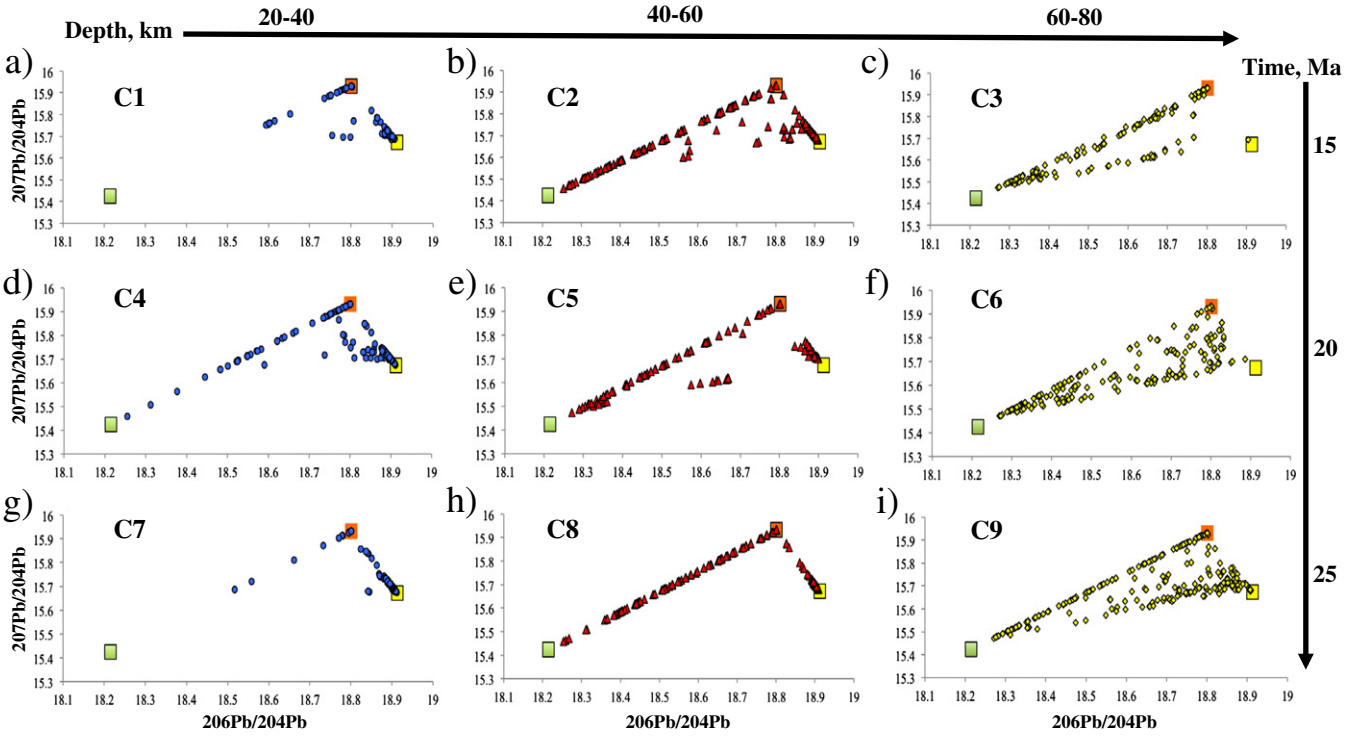

Fig. 7. Evolution of $^{207}Pb/^{204}Pb$ and $^{206}Pb/^{204}Pb$ isotopic ratios with time and depth in the hydrated/serpentinized forearc mantle during stable subduction with high fluid-related weakening. Sampling areas C1–C9 are shown in Fig. 6d–f. Solid rectangles correspond to three initial ("input") lithologies (Table 1): sediments (yellow), oceanic crust (green) and depleted dry mantle (orange). (For interpretation of the references to color in this figure legend, the reader is referred to the web version of this article.)

promoted by the increased coupling between plates, which precludes overriding plate extension irrespective of its strength (Baitsch-Ghirardello et al., 2014). In contrast to stable subduction with high fluid-related weakening (model bet51, Fig. 6), the mélange area in model bet15 ($\lambda_{fluid} = 0.05$ and $\lambda_{melt} = 0.001$) is narrow and confined to the slab interface (Fig. 9a–c). Further away from the slab, serpentinized forearc mantle is relatively undeformed and unmixed with the subducted crust (Fig. 9a–c). Its increased effective viscosity reflects the reduced degree of fluid-weakening ($\lambda_{fluid} = 0.05$). The increased coupling between the plates results in a noticeable subsidence of the forearc (Fig. 9b). Consequently, forearc basin is deeper in model bet15 than in model bet51 (cf. Figs. 6b and 9b). Plate coupling also promotes gradual thickening of the forearc lithosphere. This causes deepening of geotherms and fluid-fluxed melting zone atop the slab

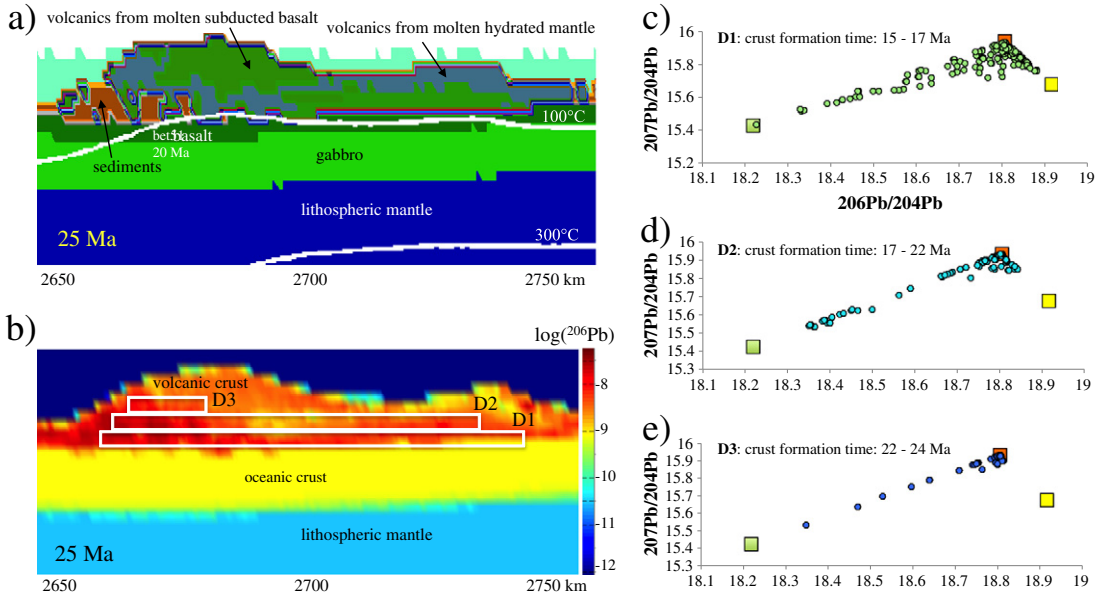

Fig. 8. Lithological structure (a) and ^{206}Pb distribution (b) in the volcanic arc crust and variations of $^{207}Pb/^{204}Pb$ and $^{206}Pb/^{204}Pb$ isotopic ratios in basaltic crust with time (c)–(e). Numerical model corresponds to stable subduction with high fluid-related weakening at 25 Ma (Fig. 6c). Sampling areas of the crust D1–D3 are shown by white rectangles in (b). Solid rectangles in (c)–(e) correspond to three initial ("input") lithologies (Table 1): sediments (yellow), oceanic crust (green) and depleted dry mantle (orange). Colors for (a) are as in Fig. 1; isotherms (white lines) are shown from 100 °C with 200 °C intervals. Time is shown since the beginning of convergence. (For interpretation of the references to color in this figure legend, the reader is referred to the web version of this article.)

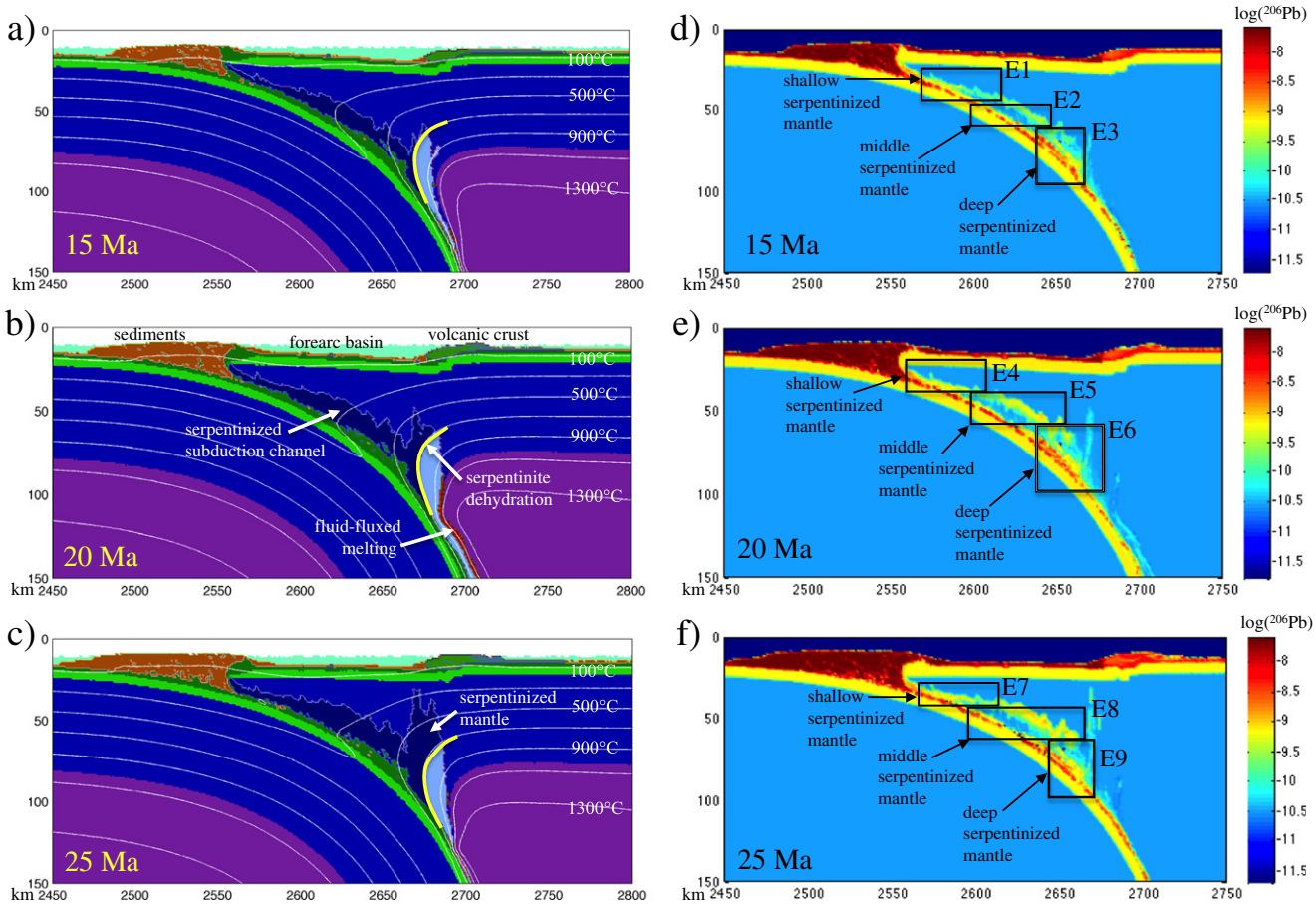

Fig. 9. Reference model for the stable subduction regime with low fluid-related weakening; ($\lambda_{fluid} = 0.05$ and $\lambda_{melt} = 0.001$, model bet15 in Fig. S1, supplement). (a)–(c) Evolution of the lithological field (colors, cf. Fig. 1) and isotherms (white lines, from 100 °C with 200 °C intervals). (d)–(f) Evolution of ^{206}Pb concentrations, black labeled rectangles E1–E9 mark hydrated mantle sampling areas for which isotopic ratios are shown in Fig. 10. Yellow lines in (a)–(c) show serpentinite dehydration. Time is shown since the beginning of convergence. (For interpretation of the references to color in this figure legend, the reader is referred to the web version of this article.)

with time (cf. Figs. 6a–c and 9a–c). In addition, narrow vertical zones of mantle serpentinization developing in the subarc lithosphere away from the slab (spike-like dark blue areas in Fig. 9a–c) have larger extent than in model bet51 (cf. Figs. 6c and 9c).

3.3.1. Pb isotopes in the mantle wedge

After 15 Ma of model evolution, a wide serpentinite area (dark blue color in Fig. 9a) has formed in the forearc region of the subduction zone. An overall increase of lead concentration is apparent in the serpentinized forearc (Fig. 9d), whereas the sediment signatures tend to decrease with increasing depth (Fig. 10a–c). The serpentinized shallow forearc mantle of subduction channel mélange formed atop the slab surface shows a slight MORB and a moderate sediment influence of isotope signatures as *double binary* MORB–mantle and mantle–sediment trends (Fig. 10a). In contrast, serpentinized middle forearc mantle is characterized by a *double binary* trend of MORB–mantle and MORB–sediment isotope signature (Fig. 10b). The deep forearc mantle shows simple *binary* MORB–mantle isotopic trend (Fig. 10c). It worth noting that the end-member signature of MORB in the middle forearc mantle is more pronounced than in both the shallow and the deep mantle (cf. Fig. 10b and a, c).

At the later subduction stages (20–25 Ma, Fig. 10d–i) changes of isotopic characteristics are only observed in the middle serpentinized forearc mantle where MORB–mantle signature gradually vanish and *binary* MORB–sediment trend become dominant (cf. Fig. 10b,e,h). Variability of isotopic characteristics in this stable subduction regime differs significantly from the previous reference models, which can be mainly related to the increased viscosity and decreased degree of mechanical mixing in the serpentinized forearc.

3.3.2. Pb isotopes in magmatic products of fluid-fluxed mantle melting

During the 25 Ma of subduction a well-developed and clearly zoned magmatic arc (Fig. 11a,b) is grown. The arc is divided in two different zones. The frontal arc zone contains large amount of volcanics derived from molten subducted basaltic crust (medium green color in Fig. 11a). In contrast, the rear arc zone, where we collected the isotope signatures, is mainly derived from fluid-fluxed melting of mantle wedge peridotite (gray color in Fig. 11a). The Pb isotope ratios in the sampled zone of the arc are dominated by the uniform steady *binary* MORB–mantle trend without any sedimentary signatures (Fig. 11c). The documented long-term stability of this simple *binary* trend differs strongly from two previous reference models and suggests negligible amount of subduction of shallow and middle serpentinized forearc mantle with sediment signatures (Fig. 10a,b,d,e,g,h) to subarc depths. Consequently, sediments-free deep forearc mantle (Fig. 10c,f,i) remains as a single source for the mantle-derived arc volcanics (Fig. 11c).

4. Discussion

We modeled numerically geochemical behavior of Pb isotopes for three different geodynamic regimes of intra-oceanic subduction (e.g. Baitsch-Ghirardello et al., 2014; Furukawa, 1993). We focused our geochemical–thermo-mechanical (GcTM) numerical study on two key "outputs" of subduction zones (e.g., Kelley et al., 2005; King et al., 2007; Marschall and Schumacher, 2012; Plank and Langmuir, 1993,

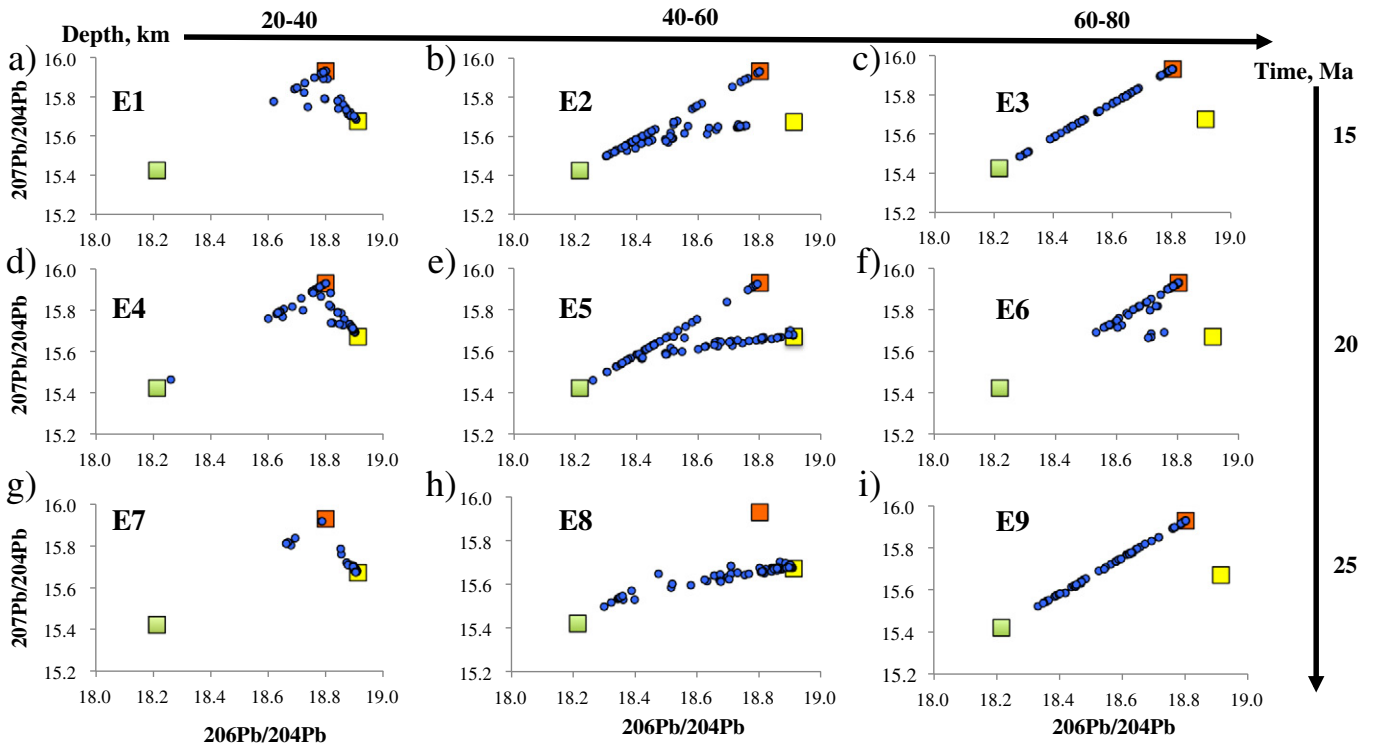

Fig. 10. Evolution of $^{207}Pb/^{204}Pb$ and $^{206}Pb/^{204}Pb$ isotopic ratios with time and depth in the hydrated/serpentinized forearc mantle during stable subduction with low fluid-related weakening. Sampling areas E1–E9 are shown in Fig. 9d–f. Solid rectangles correspond to three initial ("input") lithologies (Table 1): sediments (yellow), oceanic crust (green) and depleted dry mantle (orange). (For interpretation of the references to color in this figure legend, the reader is referred to the web version of this article.)

1998; Scambelluri et al., 2004 and references therein): (1) hydrated forearc mantle (including serpentinite mélanges) and (2) basalts derived by fluid-fluxed mantle melting. We found, that the Pb isotopic ratios in both these "outputs" are strongly heterogeneous and show five main types of geochemical mixing trends:

- *Binary* mantle–MORB trend is found in serpentinites (Figs. 4a,g, 10c,i) and volcanics (Figs. 5a,h, 8d,e, 11c).
- *Binary* MORB–sediment trend is found in serpentinites (Fig. 10h) and volcanics (Fig. 5g).
- *Double binary* mantle–MORB and mantle–sediment trends are found in shallow and middle-depth serpentinites of subduction channels (Figs. 4b,d,h, 7a,g,h, 10a,d,g).
- *Double binary* MORB–mantle and MORB–sediment trends are found in middle-depth forearc serpentinites formed by subduction with low fluid-induced weakening (Fig. 10b,e).
- *Triple* MORB–sediment–mantle mixing trend are found in deep serpentinites (Figs. 4c,e,f, 7c,f,i) and volcanics (Figs. 5b,f,g, 8c).

Three complementary mechanisms can explain these geochemical variations. First, solid/fluid partition coefficients change along the slab as the result of changes in mineralogy of dehydrating rocks (Fig. 2e,f) thus changing concentrations of lead in liberated aqueous fluids. Second, fluids of contrasting composition derived by dehydration of sediments and oceanic crust can affect the same local volumes of the forearc mantle thus causing superposition of sedimentary and MORB isotopic signatures in form of *double binary* mantle–MORB and mantle–sediments trends (Fig. 4b). Third, mechanical mixing and multiple hydration/dehydration cycles can affect deep serpentinite mélanges in the bottom of subduction channel thus producing *triple* mixing between previously formed *double binary* trends (Fig. 4c).

In agreement with geochemical data from subduction-related arcs (e.g., Guillot and Hattori, 2013; Hauff et al., 2003) all our experiments present a relatively high concentration of Pb in the volcanics from wet molten mantle (Figs. 8b, 11b). These fluid-induced signatures are ultimately derived from subducted sediments and MORB–crust and reflect high mobility of Pb (like other fluid mobile elements: Sr, As) during slab dehydration and mantle hydration processes. Our models also suggest that signatures in the magmatic arc often inherit the Pb isotope signatures of the deep hydrated forearc mantle. In some models, the signature in the deep serpentinized forearc mantle and the overlying active magmatic arc are strikingly similar (cf. Figs. 4f and 5b, 10i and 11c), which is also described in studies from natural arcs (Hattori and Guillot, 2003). Therefore the main source of Pb in the magmatic arc could be often directly linked to the subduction channel melange where mechanical and geochemical mixing takes place in the serpentinized forearc mantle (e.g., King et al., 2006; Scambelluri et al., 2004). In addition, across-arc geochemical zoning present in natural arcs (Ishikawa and Nakamura, 1994) is also observed in our models (e.g., Fig. 5b,c,e, f–i). In particular, we often observe a higher concentration of sediments-derived Pb closer to the trench than further away from the trench (cf. Figs. 5b and c). This is consistent with studies done by Ishikawa and Nakamura (1994), which described a systematically decreasing of Pb concentration in volcanic arc rocks with increasing distance from the trench.

Sedimentary isotopic signatures increase with model time in both serpentinite mélanges (e.g., Fig.7c,f,i) and volcanic arc crust (e.g., Fig. 5a,b,g). As a result, appearance of binary MORB–sediments trend without significant mantle isotopic signature is documented for mature subduction zone stages (e.g., Figs. 5g, 10h). This can be explained by growing lead concentrations in serpentinized forearc mantle with time due to continuous consumption of Pb-rich fluids originated from MORB and sediments. Consequently, fluid-added isotopic signatures overwhelm the relatively low concentrations of Pb isotopes originally present in the mantle (Table 1). This suggests that the *double binary* and *triple* mixing trends are characteristic of the early stages of subduction. In contrast, *binary* mantle–MORB and

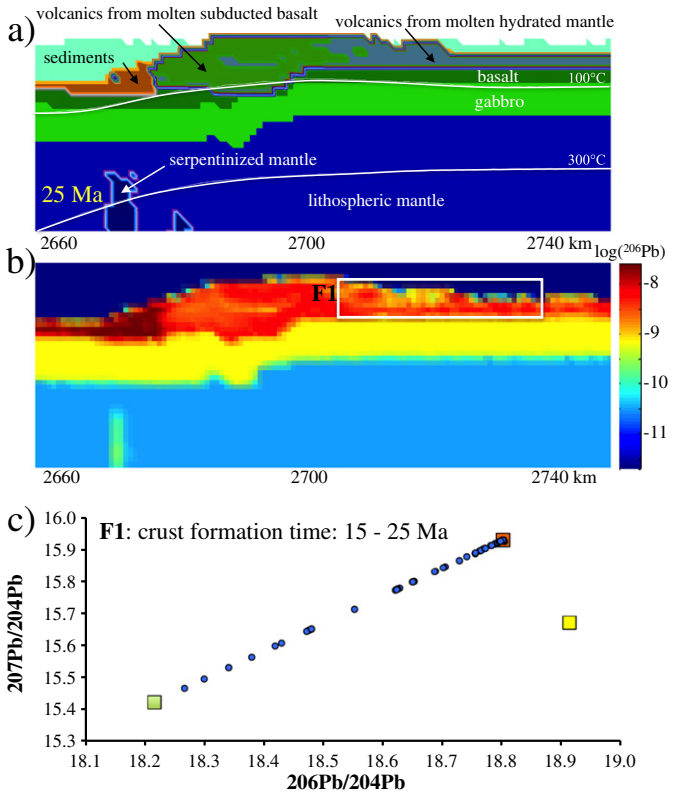

Fig. 11. Lithological structure (a) and ^{206}Pb distribution (b) in the volcanic arc crust and ^{207}Pb/^{204}Pb and ^{206}Pb/^{204}Pb isotopic ratios in basaltic crust (c). Numerical model corresponds to stable subduction with low fluid-related weakening at 25 Ma (Fig. 9c). Sampling area of the crust F1 is shown by white rectangle in (b). Solid rectangles in (c) correspond to three initial ("input") lithologies (Table 1): sediments (yellow), oceanic crust (green) and depleted dry mantle (orange). Colors for (a) are as in Fig. 1; isotherms (white lines) are shown from 100 °C with 200 °C intervals. Time is shown since the beginning of convergence. (For interpretation of the references to color in this figure legend, the reader is referred to the web version of this article.)

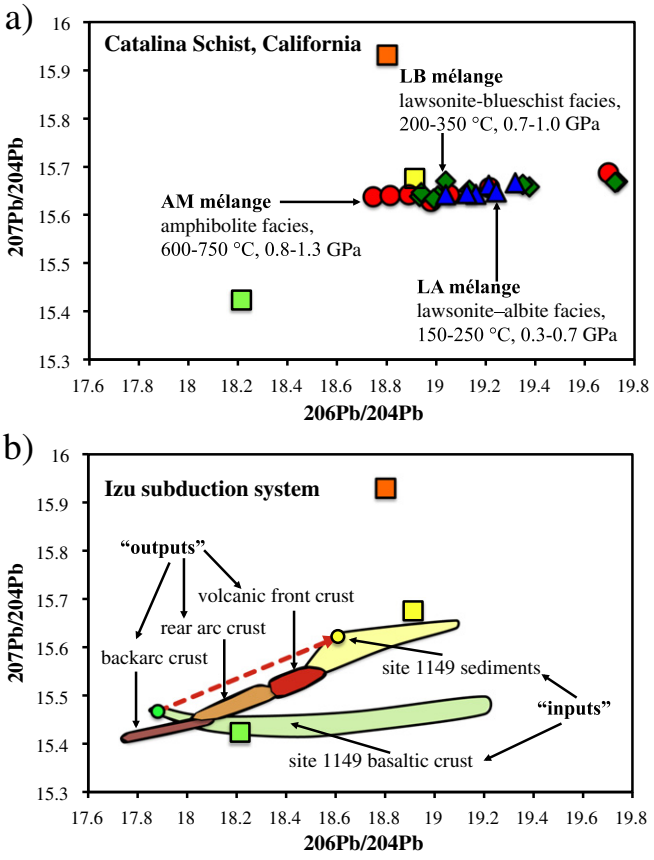

Fig. 12. Examples of nearly-binary sediments-rich isotopic mixing trends in subduction zone "outputs": (a) in Catalina Schists melanges, California (modified after King et al., 2007) and (b) in volcanic crust of Izu subduction system (modified after Hauff et al., 2003). Solid rectangles show three "input" lithologies used in our study (Table 1): sediments (yellow), oceanic crust (green) and depleted dry mantle (orange). Red dashed line in (b) show a hypothetical binary trend (Hauff et al., 2003) for mixing isotopic signatures of pelagic sediment (yellow circle) and the most unradiogenic ocean crust sample (green circle). (For interpretation of the references to color in this figure legend, the reader is referred to the web version of this article.)

MORB–sediments trends should be characteristic of mature (near steady-state) volcanic arcs with respectively low and high intensity of sedimentary melanges subduction to subarc depths (cf., Figs. 9c, 11c, 3c, and 5g). Indeed, *binary* sediment-rich isotopic mixing trends are observed in nature, for example in Catalina Schist serpentinite mélanges (e.g., King et al., 2007) (Fig. 12a) and in volcanic rocks of Izu subduction system (e.g., Hauff et al., 2003) (Fig.12b). These observations confirm the key role of geochemically hybridized serpentinized mélanges in governing geochemical evolution of magmatic arcs (e.g., Castro and Gerya, 2008; Castro et al., 2010; King et al., 2006, 2007; Marschall and Schumacher, 2012; Scambelluri et al., 2004).

5. Conclusions

Our geochemical–thermo-mechanical (GcTM) study suggests a three-stage fluid-assisted Pb geochemical transport in subduction zones: (I) from subducting dehydrating sediments and oceanic crust to serpentinite mélanges forming by hydration of the forearc lithospheric mantle, (II) from subducting dehydrating serpentinite mélanges to hydrated partially molten mantle wedge forming by fluid-fluxed melting (III) from hydrated partially molten mantle wedge to magmatic arc volcanics. The two-stage process of dehydration (sediments to melange, melange to mantle wedge) enables transportation of sedimentary isotopic signatures to subarc depths and further to arc volcanics.

Mechanical mixing and fluid-assisted geochemical transport above slabs results in spatially and temporarily variable Pb concentrations in the serpentinized forearc mantle as well as in arc volcanics. The Pb isotopic ratios are strongly heterogeneous and show five main types of geochemical mixing trends: (i) binary mantle–MORB, (i) binary MORB–sediments, (iii) double binary MORB–mantle and MORB–sediments, (iv) double binary MORB–mantle and mantle–sediments and (v) triple MORB–sediment–mantle. Double binary and triple mixing trends are transient and should be characteristic for relatively early stages of subduction. In contrast, binary mantle–MORB and MORB–sediments trends are stable and should be characteristic for mature subduction zones with respectively low and high intensity of sedimentary melanges subduction.

Acknowledgments

This work was supported by the ETH Research Grant ETH-06 09-2, CRYSTAL2PLATE Initial Training Network PITN-GA-2008-215353, 4D-ADAMELLO project PDAMP2-123074 of the Swiss National Science Foundation, and Topo-4D project 20TO21-120535 of the TopoEurope program. Constructive comments and suggestions by Marco Scambelluri and two anonymous reviewers are greatly appreciated.

Appendix A. Supplementary data

Supplementary data to this article can be found online at http://dx.doi.org/10.1016/j.lithos.2014.09.006.

References

Adam, J., Green, T., 2006. Trace element partitioning between mica- and amphibole-bearing garnet lherzolite and hydrous basanitic melt: 1. Experimental results and the investigation of controls on partitioning behavior. Contributions to Mineralogy and Petrology 152, 1–17.

Albarède, F., 2003. Geochemistry: An Introduction. Cambridge University Press.

Arevalo, R.J., McDonough, W.F., 2010. Chemical variations and regional diversity observed in MORB. Chemical Geology 271 (1–2), 70–85. http://dx.doi.org/10.1016/J. Chemgeo. 2009.12.013.

Ayers, J., 1998. Trace element modeling of aqueous fluid — peridotite interaction in the mantle wedge of subduction zones. Contributions to Mineralogy and Petrology 132, 390–404.

Baitsch-Ghirardello, B., Gerya, T., Burg, J., 2014. Geodynamic regimes of intra-oceanic subduction: implications forearc extension vs. shortening processes. Gondwana Research 25, 546–560.

Bea, F., Pereira, M.D., Stroh, A., 1994. Mineral/leucosome trace-element partitioning in a peraluminous migmatite (a laser ablation-icp_ms study). Chemical Geology 117 (293), 291–312.

Bebout, G.E., Ryan, J.G., Leeman, W.P., 1999. Fractionation of trace elements by subduction-zone metamorphism — effect of convergent-margin thermal evolution. Earth and Planetary Science Letters 171, 63–81.

Behn, M.D., Kelemen, P.B., Hirth, G., Hacker, B.R., Massonne, H.J., 2011. Diapirs as the source of the sediment signature in arc lavas. Nature Geoscience 4, 641–646.

Bostock, M.G., Hyndman, R.D., Rondenay, S., Peacock, S.M., 2002. An inverted continental moho and serpentinization of the forearc mantle. Nature 417 (6888), 536–538. http://dx.doi.org/10.1038/417536a.

Cagnioncle, A.M., Parmentier, E.M., Elkins-Tanton, L.T., 2007. Effect of solid flow above a subducting slab on water distribution and melting at convergent plate boundaries. Journal of Geophysical Research — Solid Earth 1978–2012, 112.

Carlson, R.L., Miller, D.J., 2003. Mantle wedge water contents estimated from seismic velocities in partially serpentinized peridotites. Geophysical Research Letters 30 (5), 541–544.

Castro, A., Gerya, T.V., 2008. Magmatic implications of mantle wedge plumes: experimental study. Lithos 103, 138–148.

Castro, A., Gerya, T., Garcia-Casco, A., Fernandez, C., Diaz-Alvarado, J., Moreno-Ventas, I., Low, I., 2010. Melting relations of MORB–sediment melanges in underplated mantle wedge plumes; implications for the origin of Cordilleran type batholiths. Journal of Petrology 51, 1267–1295.

Chauvel, C., Goldstein, S.L., Hoffman, A.W., 1995. Hydration and dehydration of oceanic crust controls Pb evolution in the mantle. Chemical Geology 126, 65–75.

Connolly, J.A.D., 2005. Computation of phase equilibria by linear programming: a tool for geodynamic modeling and its application to subduction zone decarbonation. Earth and Planetary Science Letters 236 (1–2), 524–541.

Davies, J.H., Stevenson, D.J., 1992. Physical model of source region of subductionzone volcanic. Journal of Geophysical Research 97, 2037–2070.

Deschamps, F., Guillot, S., Godard, M., Chauvel, C., 2010. In situ characterization of serpentinites from forearc mantle wedges: timing of serpentinization and behavior of fluid-mobile elements in subduction zones. Chemical Geology 269, 262–277.

Elkins, L.J., Gaetani, G.A., Sims, K., 2008. Partitioning of U and Th during garnet pyroxenite partial melting: constraints on the source of alkaline ocean island basalts. Earth and Planetary Science Letters 265, 270–286.

Elliott, T., 2003. Tracers of the slab. In: Eiler, J.M. (Ed.), Inside the Subduction Factory 11. American Geophysical Union, Washington, DC, pp. 23–45.

Elliott, T., Plank, T., Zindler, A., White, W., Bourdon, B., 1997. Element transport from slab to volcanic front at the Mariana arc. Journal of Geophysical Research 102, 14991–15019.

Escartín, J., Hirth, G., Evans, B., 2001. Strength of slightly serpentinized peridotites: implications for the tectonics of oceanic lithosphere. Geology 29, 1023–1026.

Ewart, A., Griffin, W.L., 1994. Application of proton-microprobe data to trace-element partitioning in volcanic rocks. Chemical Geology 117, 251–284.

Foley, S.F., Jenner, G.A., 2004. Trace element partitioning in lamproitic magmas — the Gaussberg olivine leucitite. Lithos 75, 19–38.

Foley, S.F., Barth, M.G., Jenner, G.A., 2000. Rutile/melt partition coefficients for trace elements and an assessment of the influence of rutile on the trace element characteristics of subduction zone magmas. Geochimica et Cosmochimica Acta 64, 933–938.

Furukawa, Y., 1993. Depth of the decoupling plate interface and thermal structure under arcs. Journal of Geophysical Research 98, 20005–20013.

Gerya, T., 2011a. Future directions in subduction modeling. Journal of Geodynamics 52, 344–378.

Gerya, T.V., 2011b. Intra-oceanic subduction zones. In: Brown, D., Ryan, P.D. (Eds.), Arc–Continent Collision. Frontiers in Earth Sciences. Springer-Verlag, Berlin Heidelberg, pp. 23–51.

Gerya, T.V., Meilick, F.I., 2011. Geodynamic regimes of subduction under an active margin: effects of rheological weakening by fluids and melts. Journal of Metamorphic Geology 29, 7–31.

Gerya, T.V., Yuen, D.A., 2003a. Rayleigh–Taylor instabilities from hydration and melting propel "cold plumes" at subduction zones. Earth and Planetary Science Letters 212, 47–62.

Gerya, T.V., Yuen, D.A., 2003b. Characteristics-based marker-in-cell method with conservative finite-differences schemes for modeling geological flows with strongly variable transport properties. Physics of the Earth and Planetary Interiors 140, 293–318.

Gerya, T.V., Yuen, D.A., 2007. Robust characteristics method for modelling multiphase visco-elasto-plastic thermo-mechanical problems. Physics of the Earth and Planetary Interiors http://dx.doi.org/10.1016/J.Pepi.2007.04.015 (I).

Gerya, T.V., Stoeckhert, B., Perchuk, A.L., 2002. Exhumation of high-pressure metamorphic rocks in a subduction channel — a numerical simulation. Tectonics 21 (Article Number: 1056).

Gerya, T.V., Connolly, J.A.D., Yuen, D.A., Gorczyk, W., Capel, A.M., 2006. Sesmic implications of mantle wedge plumes. Physics of the Earth and Planetary Interiors 156, 59–74.

Gorczyk, W., Willner, A.P., Gerya, T.V., Connolly, J.A.D., Burg, J.-P., 2007. Physical controls of magmatic productivity at Pacific-type convergent margins: new insights from numerical modeling. Physics of the Earth and Planetary Interiors 163, 209–232.

Gorman, P.J., Kerrick, D.M., Connolly, J.A.D., 2006. Modeling open system metamorphic decarbonation of subducting slabs. Geochemistry, Geophysics, Geosystems 7, Q04007.

Hall, P.S., Kincaid, C., 2001. Diapiric flow at subduction zones: a recipe for rapid transport. Science 292, 2472–2475.

Hattori, K.H., Guillot, S., 2003. Volcanic fronts form as a consequence of serpentinite dehydration in the forearc mantle wedge. Geology 31, 525–528.

Hauff, F., Hoernle, K., Schmidt, A., 2003. Sr–Nd–Pb composition of Mesozoic Pacific oceanic crust (Site 1149 and 801, ODP Leg 185): implications for alteration of ocean crust and the input into the Izu–Bonin–Mariana subduction system. Geochemistry, Geophysics, Geosystems 4. http://dx.doi.org/10.1029/2002GC000421.

Hawkesworth, C., Gallagher, K., Hergt, J.M., Mc Dermott, F., 1993. Trace element fractionation processes in the generation of island arc basalts. Philosophical Transactions of the Royal Society of London, Series A 342, 179–191.

Hilairet, N., Reynard, B., Wang, Y., Daniel, I., Merkel, S., Nishiyama, N., Petitgirard, S., 2007. High-pressure creep of serpentine, interseismic deformation, and initiation of subduction. Science 318, 1910–1913.

Hyndman, R.D., Peacock, S.M., 2003. Serpentinization of the forearc mantle. Earth and Planetary Science Letters 212 (3–4), 417–432. http://dx.doi.org/10.1016/S0012-821X(03)00263-2.

Ishikawa, T., Nakamura, E., 1994. Origin of the slab component in arc lavas from across-arc variation of B and Pb isotopes. Nature 370, 205–208.

Ishizuka, O., Taylor, R.N., Milton, J.A., Nesbitt, R.W., 2003. Fluid–mantle interaction in an intra-oceanic arc: constraints from high-precision Pb isotopes. Earth and Planetary Science Letters 211 (3–4), 221–236. http://dx.doi.org/10.1016/S0012-821X(03)00201-2.

Ishizuka, O., Kimura, J.-I., Li, Y.B., Stern, R.J., Reagan, M.K., Taylor, R.N., Ohara, Y., Bloomer, S.H., Ishii, T., Hargrove, U.S.I., Haraguchi, S., 2006. Early stages in the evolution of Izu–Bonin arc volcanism: new age, chemical, and isotopic constraints. Earth and Planetary Science Letters 250 (1–2), 385–401. http://dx.doi.org/10.1016/J.Eps. 2006.08.007.

Iwamori, H., 1998. Transportation of H2O and melting in subduction zones. Earth and Planetary Science Letters 160, 65–80.

Iwamori, H., 2000. Deep subduction of H_2O and deflection of volcanic chain towards backarc near triple junction due to lower temperature. Earth and Planetary Science Letters 181, 41–46.

Iwamori, H., 2004. Phase relations of peridotites under H2O-saturated conditions and ability of subducting plates for transportation of H2O. Earth and Planetary Science Letters 227, 57–71. http://dx.doi.org/10.1016/J.Epsl.2004.08.013.

Iwamori, H., Richardson, C., Maruyama, S., 2007. Numerical modeling of thermal structure, circulation of H2O, and magmatism–metamorphism in subduction zones: Implications for Evolution of Arcs. Gondwana Research 11, 109–119.

Kelley, K.A., Plank, T., Farr, L., Ludden, J., Staudigel, H., 2005. Subduction cycling of U, Th, and Pb. Earth and Planetary Science Letters 234, 369–383.

Kerrick, D.M., Connolly, J.A.D., 2001. Metamorphic devolatilization of subducted marine sediments and the transport of volatiles into the earth's mantle. Nature 411.

Kessel, R., Schmidt, M., Ulmer, P., Pettke, T., 2005. Trace element signature of subductionzone fluids, melts and supercritical liquids at 120–180 km depth. Nature 437 (724–7276835), 293–296.

Kimura, J.-I., Hacker, B.R., van Keken, P.E., Kawabata, H., Yoshida, T., Stern, R.J., 2009. Arc basalt simulator version 2, a simulation for slab dehydration and fluid-fluxed mantle melting for arc basalts: modeling scheme and application. Geochemistry, Geophysics, Geosystems 10, Q09004.

King, R.L., Bebout, G.E., Moriguti, T., Nakamura, E., 2006. Elemental mixing systematics and Sr – Nd isotope geochemistry of melange formation: Obstacles to identification of fluid sources to arc volcanics. Earth and Planetary Science Letters 246, 288–304.

King, R.L., Bebout, G.E., Grove, M., Moriguti, T., Nakamura, E., 2007. Boron and lead isotope signatures of subduction-zone mélange formation: hybridization and fractionation along the slab–mantle interface beneath volcanic arcs. Chemical Geology 239, 305–322.

Klemme, S., Prowatke, S., Hametner, K., Günther, D., 2005. Partitioning of trace elements between rutile and silicate melts: implications for Subduction Zones. Geochimica et Cosmochimica Acta 69 (9), 2361–2371.

Klimm, K., Blundy, J.D., Green, T.H., 2008. Trace element partitioning and accessory phase saturation during H2O-saturated melting of basalt with implications for subduction zone chemical fluxes. Journal of Petrology 49 (3), 523–553. http://dx.doi.org/10.1093/Petrology/Egn001.

Kodolányi, J., Pettke, T., Spandler, C., Kamber, B.S., Gméling, K., 2012. Geochemistry of ocean floor and fore-arc serpentinites: constraints on the ultramafic input to subduction zones. Journal of Petrology 53, 235–270.

Marschall, H.R., Schumacher, J.C., 2012. Arc magmas sourced from mélange diapirs in subduction zones. Nature Geoscience 5, 862–867.

McKenzie, D., O'Nions, R.K., 1991. Partial melt distributions from inversion of rare earth element concentrations. Journal of Petrology 32, 1021–1091.
Nikolaeva, K., Gerya, T.V., Connolly, J.A.D., 2008. Numerical modelling of crustal growth in intraoceanic volcanic arcs. Physics of the Earth and Planetary Interiors 171 (1–4), 336–356.
Plank, T., Langmuir, C.H., 1993. Tracing trace elements from sediment input to volcanic output at subduction zones. Nature 362 (6422), 739–743.
Plank, T., Langmuir, C.H., 1998. The geochemical composition of subducting sediment and its consequences for the crust and mantle. Chemical Geology 145, 325–394 (Doi:).
Ranalli, G., 1995. Rheology of the Earth. Chapmann and Hall, London, UK.
Ruepke, L.H., Morgan, J.P., Hort, M., Connolly, J.A.D., 2004. Serpentine and the subduction zone water cycle. Earth and Planetary Science Letters 223, 17–34.
Salters, V.J.M., Stracke, A., 2004. Composition of the depleted mantle. Geochemistry, Geophysics, Geosystems 5 (5). http://dx.doi.org/10.1029/2003GC000597 (N/A–N/A).
Scambelluri, M., Philippot, P., 2001. Deep fluids in subduction zones. Lithos 55, 213–227.
Scambelluri, M., Tonarini, S., 2012. Boron isotope evidence for shallow fluid transfer across subduction zones by serpentinized mantle. Geology 40, 907–910.
Scambelluri, M., Bottazzi, P., Trommsdorff, V., Vannucci, R., Hermann, J., Gòmez-Pugnaire, M.T., Vizcaìno, V.L.–S., 2001a. Incompatible element-rich fluids released by antigorite breakdown in deeply subducted mantle. Earth And Planetary Science Letters 192, 457–470.
Scambelluri, M., Rampone, E., Piccardo, G.B., 2001b. Fluid and element cycling in subducted serpentinite: a trace-element study of the Erro–Tobbio high-pressure ultramafites (Western Alps, NW Italy). Journal of Petrology 42, 55–67.
Scambelluri, M., Fiebig, J., Malaspina, N., Müntener, O., Pettke, T., 2004. Serpentinite subduction: implications for fluid processes and trace-element recycling. International Geology Review 46, 595–613.
Schmeling, H., Babeyko, A.Y., Enns, A., Faccenna, C., Funiciello, F., Gerya, T., Golabek, G.J., Grigull, S., Kaus, B.J.P., Morra, G., Schmalholz, S.M., Van Hunen, J., 2008. A benchmark comparison of spontaneous subduction models-towards a free surface. Physics of the Earth and Planetary Interiors 171 (1–4), 198–223.
Schmidt, M.W., Poli, S., 1998. Experimentally based water budgets for dehydrating slabs and consequences for arc magma generation. Earth and Planetary Science Letters 163, 361–379.
Sizova, E., Gerya, T., Brown, M., Perchuk, L.L., 2010. Subduction styles in the precambrian: insight from numerical experiments. Lithos 116 (3–4), 209–229.
Guillot, St, Hattori, K., 2013. Serpentinites: essential roles in geodynamics, arc volcanism, sustainable development, and the origin of life. Elements 9 (2), 95–98.
Straub, S.M., Layne, G.D., 2003. Decoupling of fluids and fluid-mobile elements during shallow subduction: evidence from halogen-rich andesite melt inclusions from the Izu Arc volcanic front. Geochemistry, Geophysics, Geosystems 4. http://dx.doi.org/10.1029/2002GC000349 (N/A–N/A).
Straub, S.M., Goldstein, S.L., Class, C., Schmidt, A., Gomez-Tuena, A., 2010. Slab and mantle controls on the Sr–Nd–Pb–Hf isotope evolution of the post 42 Ma Izu–Bonin volcanic arc. Journal of Petrology 51, 993–1026.
Tamura, Y., 1994. Genesis of island arc magmas by mantle derived bimodal magmatism: evidence from the Shirahama Group, Japan. Journal of Petrology 35, 619–645.
Tamura, Y., Ishizuka, O., Stern, R.J., Shukuno, H., Kawabata, H., Embley, R.W., Hirahara, Y., Chang, Q., Kimura, J.I., Tatsumi, Y., Nunokawa, A., Bloomer, S.H., 2011. Two primary basalt magma types from Northwest Rota-1 volcano, Mariana Arc and its mantle diapir or mantle wedge plume. Journal of Petrology 52, 1143–1183.
Tatsumi, Y., 1989. Migration of fluid phases and genesis of basalt magmas in subduction zones. Journal of Geophysical Research 94, 4697–4707.
Turner, S., Evans, P., Hawkesworth, C., 2001. Ultrafast source-to-surface movement of melt at island arcs from 226Ra-230 Th systematics. Science 292, 1363–1366.
Ulmer, P., Trommsdorff, V., 1995. Serpentine stability to mantle depths and subduction-related magmatism. Science 268 (5212), 858–861.
Vogt, K., Castro, A., Gerya, T., 2013. Numerical modeling of geochemical variations cause by crustal relamination. Geochemistry, Geophysics, Geosystems 14, 470–487.
Zack, T., 2002. Equilibrium and disequilibrium trace element partitioning in hydrous eclogites (Trescolmen, Central Alps). Journal of Petrology 43 (10), 1947–1974. http://dx.doi.org/10.1093/Petrology/43.10.1947.
Zack, T., Foley, S.F., Jenner, G.A., 1997. A consistent partition coefficient set for clinopyroxene, amphibole and garnet from laser ablation microprobe analysis of garnet pyroxenites from Kakanui. 172. Neues Jahrbuch fur Mineralogie-Abhandlungen, New Zealand, pp. 23–41.
Zack, T., Foley, S.F., Rivers, T., 2002. Equilibrium and disequilibrium trace element partitioning in hydrous eclogites (Trescolmen, Central Alps). Journal of Petrology 43, 1947–1974.